Title:

Cellular heterogeneity in pressure and growth emerges from tissue topology and geometry

Yuchen Long[1,*], Ibrahim Cheddadi[2,4], Vincent Mirabet[1], Gabriella Mosca[3], Mathilde Dumond[1,5], Jan Traas[1], Christophe Godin[1,2], Arezki Boudaoud[1,*].

1. Laboratoire Reproduction et Développement des Plantes, Université de Lyon, ENS de Lyon, UCB Lyon 1, CNRS, INRA, INRIA, F-69342, Lyon, France.

2. INRIA/CIRAD/INRA Project-team Virtual Plants, France.

3. Department of Plant and Microbial Biology, University of Zürich, Zollikerstrasse 107, CH-8008 Zürich, Switzerland.

4. Current address: Univ. Grenoble Alpes, CNRS, Grenoble INP, TIMC-IMAG, 38000 Grenoble, France.

5. Current address: Department of Biosystems Science and Engineering, ETH Zurich, Mattenstrasse 26, 4058, Basel, Switzerland.

*. Correspondence and requests for materials should be addressed to yuchen.long@ens-lyon.fr or arezki.boudaoud@ens-lyon.fr

The authors declare no competing financial interests.

Summary

Cell-to-cell heterogeneity prevails in many biological systems, although its origin and function are often unclear. Cell hydrostatic pressure, alias turgor pressure, is essential in physiology and morphogenesis, and its spatial variations are often overlooked. Here, based on a mathematical model describing cell mechanics and water movement in a plant tissue, we predict that cell pressure anticorrelates with cell neighbour number. Using atomic force microscopy, we confirm this prediction in the Arabidopsis shoot apical meristem, a population of stem cells that generate all plant aerial organs. Pressure is predicted to correlate either positively or negatively with cellular growth rate depending on osmotic drive, cell wall extensibility, and hydraulic conductivity. The meristem exhibits one of these two regimes depending on conditions, suggesting that, in this tissue, water conductivity is non-negligible in growth control. Our results illustrate links between local topology, cell mechanical state and cell growth, with potential roles in tissue homeostasis.

Key words

Cellular heterogeneity, hydrostatic pressure, tissue topology, growth mechanics, tissue hydraulics, atomic force microscopy, biophysical modelling.

Highlights

- A mechano-hydraulic model of tissue growth predicts heterogeneity in cell pressure and in cell growth according to local tissue topology.
- Indentation-based measurement of cell pressure in the shoot apical meristem of *Arabidopsis thaliana*, together with a realistic mechanical model of tissue indentation, reveals pressure variations according to cell size and cell neighbour number.
- Cell growth in the Arabidopsis shoot apical meristem either correlates or anti-correlates with cell neighbour number, which can be retrieved by the model using experimentally-based parameters.

Introduction

Cell-to-cell fluctuations are observed in many biological processes like gene expression, signalling, cell size regulation and growth [1–8]. Notably, heterogeneity in cell size and growth rate often prevails and may impact tissue patterning and macroscopic growth robustness [1,2]. Cell volume change is driven by osmosis [9–11] and the resulting intracellular hydrostatic pressure, and is restrained by peripheral constraints — plasma membrane, cytoskeletal cortex, extracellular matrix, or cell wall — in plant cells [12], animal cells [13] including tumorous [14], and microbial cells [15] (Fig. 1a).

Due to high difference between internal and external osmotic potential, cells with rigid cell walls – like in plants, bacteria and fungi – accumulate hydrostatic pressure, alias turgor pressure, often greater than atmospheric pressure (Fig. S1) [12]. Animal cells also accumulate hydrostatic pressure, especially when compacted or contracting [13,14], though to a lesser extent than walled cells. Whereas it is increasingly realized that pressure regulation is crucial for the general physiology, growth and signalling in animal [9,11,13] and plant cells [16–19], pressure remains poorly characterized in multicellular contexts.

In plants, turgor pressure drives cells expansion, which is classically modelled as visco-elasto-plastic process: irreversible expansion occurs when the pressure exceeds a threshold value and the cell deforms reversibly when pressure is smaller, as depicted in the Lockhart-Ortega equation (Fig. 1b) [20]:

$$\frac{1}{V}\frac{\mathrm{d}V}{\mathrm{d}t} = \varphi(P - P^Y)_+ + \frac{1}{E^V}\frac{\mathrm{d}P}{\mathrm{d}t}$$

where V is cell volume, P is turgor pressure, P^Y is the pressure threshold for irreversible expansion, φ is global wall extensibility (akin to inverse of viscosity) and E^V is the cell volumetric modulus, while the $_+$ index indicates that irreversible expansion occurs only if $P > P^Y$. For single cell, turgor pressure positively correlates with total growth rate (Fig. 1b). Other experimental observations in single-cell systems suggest that growth rate and pressure level are not always associated [15,21], making it difficult to assess and understand the link between growth regulation and cellular pressure build-up.

In multicellular context, like the plant shoot apex and sepal epidermis, neighbouring cells grow at notably different rates [1]. This prompts the question, according to the Lockhart-Ortega equation, of whether turgor pressure also varies between neighbouring plant cells. Intuitively, pressure difference should be equalized by plasmodesmata, symplasmic bridges connecting most plant cells [22]. This is supported by the association of plasmodesmata closing (symplasmic isolation) and pressure build-up in specialized cells, such as guard cells or cotton fibres [23–25]. However, pressure gradient was also observed in plant tissues with symplasmic continuity [26], and predicted to be crucial for perception of water availability by roots [27]. In addition, computational models of tissue mechanics suggest that neighbouring cells need to have different pressure to recapitulate tissue arrangement and mechanical status in chemical-treated Arabidopsis epidermis [28] and in Drosophila epithelia [29], although such spatial variation is yet to be demonstrated, and its relation with cell-to-cell growth variability remains elusive.

Here, we explore this issue in a model plant tissue, the epidermis of the *Arabidopsis thaliana* shoot apical meristem (SAM), by combining computational modelling, dimensional analysis, and experimental observations. Our physical model that couples tissue growth mechanics with water movement accounts for our experimental observations of turgor pressure and growth rate variability in different conditions. We show that cell pressure heterogeneity emerges from local tissue topology to influence growth variability. Pressure level, however, is not a direct predictor of growth rate, and dimensional analysis of the model reveals that growth behaviour depends on the extent of the osmotic drive and on the balance between wall extensibility and hydraulic conductivity. Together, we propose a link between cell topology and cell hydro-mechanical status that may be involved in tissue homeostasis.

Results

A mechanical-hydraulic model predicts pressure heterogeneity emerging from tissue topology

Earlier tissue models [28,29] retrieved intracellular pressure from static tissue geometry or required differential osmotic pressure, whereas a recent model by Cheddadi et al. proposed that

both pressure and growth emerge from the coupling between cell wall mechanics and classical plant hydraulics [30] in a tissue with hexagonal topology, i.e. with every cell having six neighbours. We therefore tested, based on this model, the consequences of unequal neighbour numbers on the mechanical status of the tissue, and notably on pressure (Fig. 1). We expanded on the 2D vertex model to cell walls in a multicellular tissue with more realistic 2D polygonal geometry. Generalizing the Lockhart-Ortega equation of visco-elasto-plastic 1D growth of single cell (Fig. 1b) [20], each cell wall has a thickness w and behaves as an elastic material of modulus E when wall tension induced by turgor pressure P is low enough, more specifically when the elastic strain ε (reversible deformation) is lower than a threshold ε^Y. When tension in the wall exceeds the corresponding threshold $E\varepsilon^Y$, the cell wall undergoes irreversible expansion, akin to visco-plastic flow, with an extensibility (effective viscosity) Φ^w (Fig. 1c). Water flux from extracellular space is proportional to $L^a\Delta\Psi$, where $\Delta\Psi = \Delta\Pi - P$ is the cross-membrane water potential difference (external pressure is assumed to be zero; for parsimony we set $\Delta\Pi$ constant) and L^a is the conductivity of the cell membrane. Intercellular water redistribution via plant plasmodesmata [31], animal gap junctions, or cytoplasmic bridges [32,33] is driven by intercellular differences in turgor pressure P, with a conductivity L^s. We did not prescribe turgor pressure, instead letting it emerge from local mechanical and hydraulic interplays (see STAR Methods for detailed model description).

To prescribe cell divisions, we utilized the recently introduced Willis-Refahi rule that derives from experimental data in the SAM: cells divide according to their size and to the size increment since the previous division [34]. The simulations recreate distributions of neighbour number (topological distributions) that are similar to those observed in the SAM (Fig. 1e).

We set the model parameters based on classical measurements from Boyer [35] and Cosgrove [36] (Table 1). We found turgor pressure to be heterogeneous, with a clear anticorrelation with topology: cells with less neighbours have relatively higher pressure (Fig 1f, 3 simulations, cell number $n = 1535$, Pearson correlation coefficient $R = -0.57$, $p < 10^{-100}$).

Initial parameter	Value	Initial parameter	Value
Unit length	10 µm	Apoplasmic	
Cell height h	10 µm	conductivity L^a	3.4×10^{-10} m MPa^{-1} s^{-1}
Cell wall thickness w	1 µm	Symplasmic	
Elastic modulus E	33.8 MPa	conductivity L^s	3.4×10^{-10} m MPa^{-1} s^{-1}
Wall extensibility Φ^w	2.4×10^{-5} MPa^{-1} s^{-1}	Osmotic pressure $\Delta\Pi$	0.7 MPa
Strain threshold ε^Y	0.1		

Perturbation	Modified parameter	Perturbation	Modified parameter
$\alpha^s = 0.1$	$L^s = 3.8 \times 10^{-11}$ m MPa^{-1} s^{-1}	$\theta = 10 / 3$	$\Delta\Pi = 1$ MPa
$\alpha^s = 0.9$	$L^s = 3.1 \times 10^{-9}$ m MPa^{-1} s^{-1}	$\theta = 20 / 3$	$\Delta\Pi = 2$ MPa
$\alpha^a = 0.1$	$\Phi^w = 2.2 \times 10^{-4}$ MPa^{-1} s^{-1}	$\theta = 10$	$\Delta\Pi = 3$ MPa
$\alpha^a = 0.9$	$\Phi^w = 2.7 \times 10^{-6}$ MPa^{-1} s^{-1}	$\theta = 40 / 3$	$\Delta\Pi = 4$ MPa

Table 2. Parameters used for the untreated model. (Upper) The initial parameters correspond to $\alpha^s = 0.5$, $\alpha^a = 0.5$, $\theta = 7/3$ in Figure 1f, which are based on measurements by Boyer (1985) [35] for α^a and θ, while α^s data is not available thus is conservatively ascribed an intermediate value of 0.5. (Lower) Non-dimensional parameter exploration around the reference values (initial parameters, except , $\theta = 20/3$) and the corresponding modified parameters. Note that $\alpha^a = 0.9$ corresponds to measurements by Cosgrove (1985) [36], compiled by Ortega (2019) [37].

In order to test the robustness of this result, we explored the parameter space of the vertex model. Analytical exploration in a two-cell system [30] had showed that systems dynamics is mostly controlled by three dimensionless parameters. The first, α^s, compares intercellular water conductivity to total (intercellular and transmembrane) conductivity,

$$\alpha^s = \frac{A^s L^s}{A^s L^s + A^a L^a}$$

with A^a the average surface of a cell, A^s the average surface of a cell in contact with neighbouring cells, L^a the conductivity (per unit surface) of the plasma membrane, and L^s the conductivity (per unit surface) due to plasmodesmata. The second, α^a, compares the limitation of growth by transmembrane conductivity to the combined limitation of growth by cell wall extensibility and transmembrane conductivity,

$$\alpha^a = \frac{L^a}{L^a + \Phi^w \frac{h^2}{4w}}$$

where h and w are cell height and cell wall thickness. Both α^s and α^a are bound between 0 and 1. The third parameter, θ, assesses the osmotic drive by comparing the cross-membrane osmotic pressure difference, $\Delta\Pi$, and a representative threshold pressure for growth to occur, P^Y,

$$\theta = \frac{\Delta\Pi}{P^Y}$$

Contrary to the Lockhart-Ortega model that was formulated at cell scale, our model accounts for specific cell wall geometry and mechanical properties. Accordingly, we express the threshold in terms of a yield strain ε^Y and the threshold pressure depends on cell geometry and topology. We found empirically [30] that half the threshold pressure of a single hexagonal cell provides a good order of magnitude for the threshold pressure in the multicellular model and hence use

$$P^Y = \frac{w}{2R\cos(\pi/N)} E\varepsilon^Y$$

where R is a representative cell size and the number of cell neighbours is $N = 6$ (Fig. S1). The tissue globally grows if θ is greater than 1. Our first results, obtained with $\alpha^s = 1/2$, $\alpha^a = 1/2$, and $\theta = 7/3$, corresponded to a balance between mechanical and hydraulic limitations to growth (Fig. 1f). We explored the parameter space by considering 4 values of θ reaching up to 40/3 (Fig. 1i, S2). As will be clarified below (see last subsection), we considered $\theta = 20/3$ as a reference value (Fig. 1g). We then decreased and increased either α^s or α^a down to 0.1 or up to 0.9, respectively (Fig. 1i, S2). Note that the values 0.5 and 0.9 of α^a span available measurements of extensibility and conductivity [35,36] (Table 1). Next, we tested the effect of cell divisions by arresting them (Fig. 1h). In all cases, we recovered the turgor–neighbour-number anticorrelation (Fig. 1f-i, S2), demonstrating that topology-related pressure heterogeneity is a robust behaviour of the model.

In simulations, like in SAM surface, cell neighbour number and size are coupled (Fig. 1f-i, S2).

168 Consistently, cell-specific turgor pressure anticorrelates with normalized cell area (Fig. 1f-I,
169 S2). To uncouple cell size and topology, we modified the initial state of our simulation to have
170 four-neighboured cells bigger than eight-neighboured cells, and found that higher turgor
171 pressure accumulated in four-neighboured cells, not in the smaller cells (Fig. 1j), showing that
172 turgor pressure heterogeneity emerges from tissue topology rather than cell size differences.
173 This can be explained by local topology, which determines cell wall angles and the subsequent
174 tension distribution at each tricellular junction (Fig. 1k, l): in our model, wall stress and strain
175 above the growth threshold are relaxed at a rate limited by wall extensibility and hydraulic
176 conductivity. Therefore, stress and strain are relatively homogenised in non-dividing
177 simulations (Fig. 1h), and the sum of wall tension at each tricellular junction (vertex) mostly
178 depends on the angles between walls. The vertex between three hexagonal cells with 120°
179 internal angles has a sum of tension at zero (Fig. 1k). Fewer-neighboured cells have sharper
180 internal angles, so the sum of tension at vertex is greater towards the cell interior, creating
181 additional inward compression and prompting higher pressure build-up at equilibrium (Fig. 1l).
182 In dividing simulations, new walls do not bear stress right after division because they form from
183 cell interior. These new walls are gradually strained due to mesh growth but do not yield
184 (expand) to release stress before reaching the threshold (Fig. 1f, g). Consequently, cell division
185 keeps the wall stress from homogenizing and dampens the turgor–neighbour-number
186 anticorrelation, compared to non-dividing simulations (Fig. 1g).

187 Altogether, our results imply that local hydrostatic pressure heterogeneity does not require
188 differential cellular osmotic pressure [28] in a growing tissue, and predict a topological origin
189 of pressure variability.

190 **Atomic force microscopy reveals heterogeneous turgor pressure in Arabidopsis shoot**
191 **apical meristem**

192 To test predictions, we built upon recent advances in atomic force microscopy (AFM) that
193 enabled non-invasive turgor pressure retrieval utilizing indentation force-displacement and
194 surface topography in living plant cells (Fig. 2) [38–42]. We used a pressurized thin-shell model
195 to deduce the turgor pressure value from the AFM-measured force-displacement curves, which
196 are influenced by turgor pressure, cell wall mechanical properties, cell 3D geometry [38], and

may reflect mechanical properties at different sub- to supra-cellular scales according to indentation depths (Fig. 2b-e). We applied AFM measurements to the Arabidopsis SAM epidermis, a system featuring substantial growth heterogeneity [1]. We included untreated soil-grown SAMs (Fig. 3) and a conceptually simpler model SAM co-treated with naphthylphthalamic acid (NPA), a polar auxin transport inhibitor that induces pin-formed SAMs, and oryzalin, a microtubule-depolymerizing drug that blocks cell division but permits continuous, isotropic growth; hereafter referred to as "oryzalin-treated SAMs" (Fig. 4) [28]. Walls between cells are often curved in growing oryzalin-treated SAMs, suggesting that neighbouring cells have different turgor pressure [28] in a growing tissue.

Figure 2 illustrates the AFM measurement pipeline, where we determined SAM surface topography with AFM (Fig. 2f) and performed indentations near the cell centre to have near-perpendicular indentation and minimize any bias due to surface slope (Fig 2g). Physical values required to deduce pressure using the published formula [39,40], except cell wall thickness separately measured by electron microscopy (EM), are simultaneously determined by AFM scan and indentation. Specifically, both mean curvature κ_M and Gaussian curvature κ_G of outer cell walls directly contribute to the capacity to sustain turgor pressure [38,39,43], and were determined from AFM scan topography (Fig. 2f). As previously suggested in tomato SAM [44], outer periclinal wall thickness is not very variable between cells or within cells in Arabidopsis SAM, with untreated meristem t_u = 179 ± 7 nm (mean ± standard error of mean, SEM) and oryzalin t_o = 742 ± 29 nm (Fig. S3). Based on previous work [45], we used the indentation depth range 0 to 150 nm to determine apparent Young's modulus of cell wall, E (Fig. 2b, e). We determined indentation stiffness, k, using the depth range 0.3 to 0.5 μm for untreated and 1.1 to 1.5 μm for oryzalin-treated meristems (Fig. 2c, e); these ranges were chosen so that depth is greater than wall thickness (to minimize cell wall contributions to k) and the deformed region remains smaller than cell size (to minimize the contributions of neighbouring cells to k, Fig. 2d, e), so as to be in the validity range of the pressurized shell model [40]. Note that these values of depth for untreated SAMs differ from the larger values (1 to 2 μm) used in preliminary experiments [41], which were interpreted using supracellular curvature (unlike here) and were chosen to reveal supracellular pressure (averaged over many cells and possibly over cell layers)

226 for comparison with the large-scale pressure obtained using indentation with a large flat tip
227 (100 μm diameter). To verify the validity of the depth ranges used here, we tested influence of
228 tissue context on indentation readout [46] by numerical simulations of indentations on realistic
229 3D meshes accounting for pressurized epidermal cells (Fig. 2m-o''); in conditions
230 corresponding to experiments, the deformation of neighbouring cells was negligible,
231 demonstrating that the depth range enables cell-level measurements.

232 Cell-specific AFM indentations on seven untreated and nine oryzalin-treated SAMs revealed
233 that surface wall curvature, Young's moduli, cell apparent stiffness and the deduced turgor
234 pressure are all markedly heterogeneous across SAM epidermis (Fig. 3, 4). We computed
235 intracellular variability of quantities measured at subcellular scale (which excludes curvature,
236 measured at cell scale), and found that apparent Young's modulus E and stiffness k show
237 significantly higher variability than pressure P (as quantified by intracellular coefficients of
238 variation, Fig. 3i, 4i), which agrees with previous work [40], and supports deduced P being a
239 cellular property. Additionally, we found that E shows relatively comparable subcellular and
240 intercellular variability, as previously observed [45,47], whereas P show significantly bigger
241 heterogeneity between than within cells (Fig. 3j, 4j). Deduced pressure, P, is relatively
242 insensitive to variability in thickness as described in [40], and change in thickness by 1×
243 standard deviation (SD) only alters the coefficient of variance (CV) of P by 3% and 9% for
244 untreated and oryzalin-treated samples respectfully, both significantly smaller than the
245 intercellular P variability (untreated 21% and oryzalin 15%). All these indicate that P deduction
246 is cell-specific, and that variability in cell wall mechanics does not account for deduced pressure
247 heterogeneity.

248 **Osmotic treatments reveal large values of osmotic pressure in the shoot apical meristem**

249 Based on AFM, we find that deduced turgor pressure is heterogeneous, with averages values
250 per meristem of 2.61 ± 0.03 MPa and 1.21 ± 0.34 MPa (mean ± SEM) in untreated and oryzalin-
251 treated meristems, respectively (Fig. S3). These values appear high with respect to the classical
252 0.3 to 1 MPa range found in most other plant tissues, though values of up to 5 MPa were
253 measured in guard cells of other species using the pressure probe [48].

254 As neither the classic pressure probe nor the pico gauge [49] can be applied to cells as small as
255 in the shoot apical meristem, we assessed quantitatively the values of turgor pressure P, by
256 using an incipient plasmolysis assay to determine the osmotic pressure of SAM, and found that
257 untreated meristems had a rather invariable osmolarity of about 0.5 Osm, slightly higher than
258 values reported in tomato SAM [50], while oryzalin samples showed a wider variability of 0.6
259 to 1.0 Osm (Fig. S4). The corresponding values of osmotic pressure, 1.2 MPa for untreated and
260 2.0 MPa for oryzalin treated, are comparable to the values of AFM-deduced turgor (2.6 MPa
261 and 1.2 MPa, respectively) (Fig. S3, S4). The quantitative agreement is less good in the case of
262 untreated meristems, possibly due to tissue tension in the epidermis which could artificially
263 increase the deduced pressure due to contributions from inner layers. We note however that
264 tissue tension would smooth out intercellular differences and would thus not contribute to the
265 cell-to-cell heterogeneity of pressure. An alternative explanation would be that solute
266 penetration differs between untreated and treated SAMs. Altogether, the values of turgor found
267 with AFM are in semi-quantitative agreement with the values of osmotic pressure deduced from
268 incipient plasmolysis.

269 **Cell pressure in shoot apical meristem anticorrelates with local topology and size**

270 Next, we tested model predictions and found that, indeed, AFM-determined cellular pressure
271 anticorrelates with the number of epidermal cell-neighbours N, or local topology (7 SAMs, n =
272 503 cells, R = -0.16, p = 10^{-4}, Fig. S5). With the linear relationship between cell area and
273 neighbour number (Fig. 3d) due to fundamental geometrical constraints in compact tissues [51],
274 we also identified strong anticorrelation between pressure and cell size A (R = -0.19, p = 10^{-5}).
275 We focused on cell-to-cell turgor variations and we removed variations between SAMs by
276 normalizing cellular pressure to the average pressure per SAM; given that untreated SAMs have
277 unvaried average turgor values (Fig. S3), the anticorrelation is conserved for pressure-versus-
278 topology (R = -0.16, p = 10^{-4}) and versus-size (R = -0.23, p = 10^{-7}) (Fig. 3h-h").

279 Encased in rigid cell walls, plant cells seldom exchange neighbours, and the main source of
280 topological change is via division, where dividing cells tend to lose neighbours and cells
281 adjacent to the division plain tend to gain neighbours [52]. We therefore considered oryzalin-
282 treated SAM, in which cell divisions are arrested while growth is continuous, and recovered

similar anticorrelation for pressure against neighbour number (9 SAMs, n = 202 cells, R = -0.19, p = 0.008) and against cell area (R = -0.48, $p = 10^{-12}$) (Fig. S5). Normalization further enhanced the pressure-versus-topology anticorrelation (R = -0.31, $p < 10^{-5}$) while preserving the pressure-size trend (R = -0.33, $p < 10^{-5}$) (Fig. 4h-h''), indicating that the pressure-topology and pressure-size relationships are robust system-level trends, regardless of the absolute values.

We then examined whether such trends may be caused by trends in cell wall thickness, t, or modulus, E, or by trends in stiffness, k. There is no correlation between t and cell size (R = -0.10, p = 0.65, Fig. S3). So t only introduces small unbiased noise, and it cannot account for the P heterogeneity. We found that E and k showed no significant correlation to cell neighbour number N in untreated SAMs (Fig. 3e-f'), indicating that they introduce no systemic bias to P heterogeneity. In oryzalin-treated SAMs, however, both E and k showed weak positive correlation to N (Fig. 4e-f'), which is opposite to the P vs N anticorrelation (Fig. 4h'). This is interesting, because the higher P in N = 4 cells cannot be explained by lower E and k ("softer" cell). This indicates that, although feedback from shape on E may occur in oryzalin-treated meristems, P heterogeneity is not a direct consequence of feedbacks from wall tension or cell geometry/topology on wall stiffness.

Moreover, we found that turgor pressure heterogeneity may be removed when sample is osmotically challenged: the same SAM shows heterogeneous pressure when turgid and homogeneous pressure when at intermediate turgidity (Fig. S4). This shows that the AFM approach is not technically biased by tissue topology and/or cell size.

Finally, we used cell side wall convexity as a proxy for differences in turgor, because cells with higher pressure would be expected to bulge out into cells with lower pressure (Fig. 4q-q'') [53]. We constructed a weighed convexity index (wCI) to quantify convexity (Fig. 3o-q, 4o, p), and found that convexity significantly anticorrelates with number of neighbours, in agreement with qualitative observations in oryzalin-treated meristems [28], and in agreement with the pressure trends.

Altogether, our data indicate that non-random turgor pressure heterogeneity establishes in tissues with static topology (no neighbour number change) or dynamic topology (neighbour

numbers change due to division). Although tissue topology is sufficient to explain pressure heterogeneity, we do not exclude a role of other biological parameters and/or sources of noise in pressure variations, as suggested by weaker correlations in experiments (Fig. 3h', 4h') than in simulations (Fig. 1g, h).

Realistic mechanical models of tissue indentation are inconsistent with homogeneous pressure

Whereas the aforementioned pressure deduction is based on a model utilizing local cell shape [39], Mosca et al. [46] proposed that cell packing also contribute to the indentation stiffness. We therefore implemented realistic indentation using a thin-shell indentation finite element method (FEM) model following Mosca et al. [46]. We constructed two realistic templates (untreated- and treated-like) from confocal images; the surface was meshed and the outermost cell layer was constructed to represent the epidermis, with uniform values of cell wall thickness taken from our EM-based measurements and same cell dimensions as in confocal images; all cells were inflated by turgor pressure (Fig. 2m). We used the null hypothesis that all cells were inflated by uniform turgor pressure (2 MPa, rounded from experimental values), and performed indentations on the exact corresponding cells indented experimentally from these two templates, excluding cells at periphery of the template to avoid boundary effects. We chose indentation near the cell centre to have near-perpendicular indentation, like in experiments. We recovered values of apparent stiffness k that have the same magnitude as experimental values: untreated-like k_{FEM} = 14.9 ± 0.1 N/m (mean ± SEM, compared to k_{AFM} = 12.9 ± 0.2 N/m), treated-like k_{FEM} = 38.2 ± 1.0 N/m (compared to k_{AFM} = 14.5 ± 0.6 N/m). However, we found that the k variability differs from experiments, notably in untreated SAMs (Fig. 3k, 4k). Closer inspection revealed that cell surface mean curvature κ_{M}, which is directly linked to P, also showed strong discrepancy between simulation and experiment (Fig. 3l, 4l). Accordingly, the null hypothesis of uniform turgor is not consistent with experimental data. We corrected such discrepancy based on the theory of thin shells (apparent stiffness mainly depends on these two parameters following $k \sim \pi P \kappa_{\mathrm{M}}^{-1}$, see [39]) by rescaling κ_{M} and P according to their experimental variability, and recovered the heterogeneous distribution of k determined by AFM (Fig. 3m, 4m). Conversely, correction of k and κ_{M} also recovered the experimentally deduced P

distribution. This indicates that the discrepancy between FEM and AFM indentations can be fully explained by the heterogeneity in pressure (and subsequently curvature), and the contribution of cell packing to the measured variability is negligible with our depths of indentation.

Two types of correlations between cell growth and local topology or size

Next, we monitored areal growth rate of SAM epidermal cells by time-lapse confocal microscopy. As observed previously, untreated SAMs exhibited slower growth in the centre, where stem cells reside, than the surrounding cell [54] (Fig. S5). In addition, cellular growth rate anticorrelates with neighbour number (11 SAMs, n = 1491 cells, R = -0.15, $p = 10^{-8}$; Fig. 5e) and cell size (Fig. 5f; R = -0.33, $p = 10^{-38}$), supporting previous reports that smaller cells in SAM grow faster [34,55], and suggesting that higher turgor pressure in fewer-neighboured cells associates with faster growth. In oryzalin-treated SAMs, however, the fewer-neighboured and small cells grew slower (14 SAMs, n = 1160 cells; Fig. 5k, neighbour number R = 0.20, $p = 10^{-11}$; Fig. 5l, cell size R = 0.16, $p = 10^{-8}$). This suggests that higher turgor pressure associates with either faster or slower growth depending on conditions. Although seemingly a small shift, this negative-to-positive slope change of local growth heterogeneity captures a strong qualitative inversion of growth behaviour (Fig. 5d, j). Accordingly, smaller cells expand more than larger cells in untreated SAMs, which may contribute to cell size homeostasis, a phenomenon that would be absent in oryzalin-treated SAMs.

Heterogeneity in growth rate is patterned according to the balance between wall extensibility, tissue conductivity and osmotic drive

We further explored the growth trend in our vertex model. Based on the parameter exploration on dividing mesh aimed to reproduce untreated SAM behaviour, we found both positive and negative correlations between growth rate and cell neighbour number (Fig. S2). This indicates that growth trend is sensitive to parameters that alter the balance between water flux and wall expansion (governed by the non-dimensional parameter α^a) and to the ratio between osmotic pressure and yield pressure ($\theta = \Delta\Pi / P^Y$). This can be rationalized by examining the relative growth rate G of a cell according to the Lockhart model (see [30]).

$$G = \alpha^a \Phi^w \frac{h}{2w}(\Delta\Pi - P^Y)$$

Both the prefactor $\alpha^a \Phi^w h/2w$ and the yield pressure P^Y decrease with cell size R and neighbour number N, while $\Delta\Pi$ is constant. Consequently two regimes are expected: when the osmotic drive θ is smaller than a threshold θ^T, G is dominated by the variations of P^Y, therefore G increases with cell size and with neighbour number, which corresponds to the trend in oryzalin-treated meristems; when $\theta > \theta^T$, the variations of P^Y are negligible, so G follows the prefactor and decreases with cell size, which corresponds to the trend in untreated meristems. These two regimes occur whatever the value of α^a, and the threshold value θ^T increases with increasing α^a. In a tissue context, many global parameter shifts can invert growth trend through changes in these dimensionless parameters (Fig. 6k, l).

Overall, the model retrieves untreated SAM trends if transmembrane conductivity partially limits growth (α^a not too large), symplasmic conductivity is not on par with transmembrane conductivity (α^s not too large) or if the osmotic drive is sufficient (the ratio of osmotic to yield pressure is large enough). Conservatively, we chose equal contribution by flux and wall in our model (α^a = 0.5), and increased osmotic pressure to 2 MPa, a value comparable to the experimental measurements: Figures 6a-c show that the fewer-neighboured and smaller cells grow faster (3 simulations, n = 1496; G vs N, R = -0.10, $p = 10^{-4}$; G vs A, R = -0.76, $p < 10^{-100}$).

We then attempted to reproduce oryzalin-treated behaviour, guided by the experimental observations that, besides stopping cell division, oryzalin treatment also yields higher osmotic pressure (1.6-fold) and drastically thicker cell walls (4-fold) (Fig. S3, S4). We found that both stalling division and increasing osmotic pressure failed to invert the growth trend in the model, as expected, while doubling and quadrupling wall thickness inverted the correlation of growth rate to neighbour number and cell size (Fig. 6d-j; S6), like in oryzalin-treated SAM. Combining higher osmotic pressure and thicker wall revealed that quadrupling wall thickness can robustly trigger growth trend inversion (Fig. 6j, S6).

Effectively, changing osmotic pressure and wall thickness alter the wall–flux limitation balance of the system (Fig. 6j-l). Higher osmotic pressure induces faster water influx (reduced limitation

395 by hydraulics). The extra volume strains the walls to accumulate stress farther beyond the
396 threshold, which is relaxed by wall yielding (growth) with extensibility as the rate limit.
397 Meanwhile, wall thickening reduces wall stress and strain towards the threshold for expansion,
398 effectively reducing the mechanical drive of growth and increasing the weight of water
399 permeability in limiting growth. We do not exclude other possible parameter changes triggered
400 by oryzalin treatment, like water conductivity and wall synthesis rate, that also contribute to the
401 wall–flux limitation balance. Nevertheless, implementing the observed cell wall thickening in
402 the model is sufficient to explain the observed growth rate inversion from untreated to oryzalin-
403 treated scenario.

404 **DISCUSSION**

405 In this study, we modelled the growth of a plant tissue by coupling tissue mechanics and tissue
406 hydraulics. This generalizes previous models focusing only on mechanics [56–58]. In this
407 model, both cell growth and turgor pressure emerge from mechanics and hydraulics. Each of
408 these parameters can be controlled by genetic and biochemical inputs, and small uniform
409 changes in these biological inputs can enable drastic shifts of system behaviour and the final
410 cell size distribution (Fig. 6m). We predicted that a broad distribution of neighbour number
411 leads to heterogeneity in cell growth and in turgor pressure, even when hydraulics has a minor
412 contribution to the control of growth. We verified this prediction in the context of the shoot
413 apical meristem (SAM) of *Arabidopsis thaliana*. It remains to be seen whether our results apply
414 to other plant tissues, to animals or whether this is specific to the SAM.

415 In order to test our predictions and deduce pressure in the SAM, we combined a recently
416 developed indentation-based approach [40] with FEM-based realistic mechanical models of
417 indentation [46]. We found values of turgor in the range 1-3 MPa range, higher than the range
418 0.2-1 MPa generally measured in plant tissues [18], though values of up to 5 MPa were
419 measured in guard cells [48]. For instance, the Arabidopsis root epidermis has a turgor of about
420 0.4 MPa, as measured with the pressure probe [59]; the Arabidopsis leaf epidermis has a turgor
421 of about 1-2 MPa, as deduced form indentation and mechanical modelling [60]. Accordingly,
422 we speculate that the SAM function might require relatively high turgor. Another specificity of

423 the SAM could be a relatively low transmembrane conductivity, as most aquaporin (channel
424 protein allowing rapid transmembrane water flux [61]) isoforms had significantly lower
425 expression in inflorescence than in other fast growing tissues like stem and root [62] (with a
426 reduction up to ~80%). Nevertheless, a wide range of water conductivity can produce pressure
427 heterogeneity, including very high conductivity (i.e. $\alpha^a = 0.9$ [36]), and the agreement between
428 model predictions and experimental measurements suggest that tissue hydraulics has a
429 (possibly small) contribution to limiting growth in the SAM. Similarly, altered expression of
430 the aquaporin PIP2;1 delays the emergence of lateral roots [63], also hinting to a developmental
431 role for hydraulic conductivity. Altogether, we propose that tissue mechanics and hydraulics act
432 in parallel with the established genetic regulations in SAM cell growth.

433 We found that both cell growth and turgor pressure are heterogeneous in the SAM. It has already
434 been reported that smaller cells [55] or the smaller of two sister cells [34] grow faster in the
435 SAM of untreated and NPA-treated plants, respectively. We found the same trend in untreated
436 SAM, with an inversion in oryzalin-treated SAM. Such inversion is not irrelevant to normal
437 development: for example, a growth variability switch is observed during sepal development,
438 where clones of smaller and often fewer-neighboured cells grow faster in young sepals then
439 slower in older sepals, effectively shifting from homogenizing to amplifying cell size variability
440 [64]. In untreated SAM, small cells grow faster than big cells, possibly contributing to tissue
441 homeostasis. Finally, irrespective of the conditions, we find that turgor pressure is smaller in
442 big cells in experiments, which might contribute to reducing mechanical stress in the cell wall
443 in these cells [65]; this would act in parallel with the mechanism proposed in the context of leaf
444 epidermal cells, based on cells adopting puzzle shapes that limit cell wall stress [65].

445 Our results point towards a link from cell topology (number of neighbours) to cell mechanical
446 status. This might also be relevant to animal epithelia [29], though this appears unexplored
447 experimentally. Feedbacks from cell mechanics to cell topology are more established: cell
448 division and thus number of neighbours can be oriented by mechanical stress in animals and in
449 plants [66–69]. Since tissue topology is highly conserved in many biological systems [70], we
450 propose that pressure heterogeneity may emerge in compact tissues with polygonal cells [63]
451 and non-instantaneous water movement, due to the adjustment to reconcile local mechanical

452 and hydraulic conditions.

453 Finally, we note that heterogeneous patterns may not always be stochastic [71]. The emergent
454 heterogeneity of local growth and hydrostatic pressure is coupled with the characteristic yet
455 dynamic tissue topology [51,52] (Fig. 6m), all based on stringent rules and likely underlies
456 morphogenesis in compact tissues. With the discovery of many cell-size-dependent transcripts
457 [3,72], our model proposes another source for non-random variability in a tissue.

458

459

460 **STAR Methods**

461 **Plant materials, treatments and growth conditions**

462 *Arabidopsis thaliana GFP-LTi6b* (ecotype WS-4) reporter line and ecotype Col-0 was used[73].
463 Untreated inflorescence meristems were obtained from soil-grown plants, first in short-day (8
464 h light 20°C / 16 h dark 19°C cycle) for 3 to 4 weeks then transferred to long-day (16 h light
465 20°C / 8 h dark 19°C cycle) for 1 to 2 weeks to synchronize bolting. Oryzalin-treated
466 inflorescence meristems were obtained from plants grown on custom-made Arabidopsis
467 medium [74] (Duchefa) supplemented with 1% agar-agar (Merck) and 10 µM N-1-
468 naphthylphthalamic acid (NPA, Sigma-Aldrich/Merck) for 3 weeks. Pin-formed inflorescence
469 meristems from NPA medium were immersed in 10 µg/mL oryzalin (Sigma-Aldrich/Merck)
470 twice (3 h duration, 24 h interval) [28]. For mechanical measurements and time-lapse confocal
471 imaging, meristems were mounted on Arabidopsis apex culture medium (ACM) [74] with 2%
472 agarose and 0.1% plant preservation mixture (PPM, Plant Cell Technology) to prevent
473 contamination, and cultivated in long-day condition.

474 **Atomic force microscopy**

475 Untreated meristems (dissected, with most late stage-2 floral primordia removed to prevent
476 blocking of the cantilever) and oryzalin-treated meristems were mounted on ACM (2% agarose,
477 0.1% PPM) the night before. Drops of 2% low melting agarose (Duchefa) were applied around

478 the lower parts of meristems for mechanical stabilization. For oryzalin-treated meristems, 72 h
479 post-treatment meristems were measured.

480 AFM indentations were performed as in Beauzamy et al., 2015 [40]. Specifically, a BioScope
481 Catalyst model AFM (Bruker) operated with the NanoScope software (version 9.1, Bruker),
482 under a MacroFluo optical epifluorescence macroscope (Leica), was used. All measurements
483 were done with customized 0.8 μm diameter spherical probes mounted on silicon cantilevers
484 of 42 N/m spring constant (SD-Sphere-NCH-S-10, Nanosensors). Cantilever deflection
485 sensitivity was calibrated against a clean sapphire wafer submerged in water before each session.

486 Meristems were submerged in water during AFM measurements. PeakForce QNM mode was
487 used to record sample surface topography and cell contours (aided by the stiffness difference
488 between periclinal and anticlinal cell walls on DMT modulus maps) in overlapping square tiles
489 of 30×30 to 50×50 μm^2 (128×128 pixels). Force curves were obtained by the point-and-shoot
490 mode of the NanoScope software, with at least 3 locations chosen near the barycentre of each
491 cell, and 3 consecutive indentations per location, making at least 9 force curves per cell.
492 Approximately 10 μN maximum force was applied during each indentation, corresponding to
493 approximately 1 μm indentation depth.

494 For hyperosmotic treatments, oryzalin-treated meristems were mounted in Petri-dishes on
495 Patafix (UHU), then the gap between Patafix and sample base was quickly sealed with bio-
496 compatible glue Reprorubber-Thin Pour (Flexbar) for stabilization. After the glue solidified
497 (less than 2 minutes), samples were submerged in liquid ACM containing 0.1% PPM. Samples
498 were first measured in liquid ACM (plus 0.1% PPM), then submersion medium was changed
499 to ACM plus desired concentration of NaCl (plus 0.1% PPM) by first rinsing with 3~5 mL
500 target solution, then soaked in target solution for 5 minutes before AFM measurements. Each
501 new measurement per solution change took around 30 minutes.

502 **Force curve analysis**

503 Turgor pressure was determined as previously reported [40]. Specifically, cell wall elastic
504 modulus (Hertzian model, 1~10% maximal indentation force) and cell apparent stiffness (linear,
505 75~99% maximal indentation force) were retrieved from each force curve by the NanoScope

506 Analysis software (version 1.5, Bruker). Quality of force curves were checked empirically and
507 by the fit coefficient of determination $r^2 > 0.99$. Cells with only low quality force curves were
508 not analysed. Cell surface curvatures (mean and Gaussian) were estimated from AFM
509 topographic images, with the curvature radii fitted to the long and short axes of each cell. Turgor
510 pressure was further deduced from each force curve (100 iterations) with the electron-
511 microscopy-determined cell wall thickness 190 nm for untreated and 740 nm for oryzalin-
512 treated SAMs, and cell-specific turgor pressure is retrieved by averaging all turgor deductions
513 per cell.

514 For cell registration, confocal stacks of each meristem were obtained prior to AFM
515 measurements by an LSM 700 confocal (Carl Zeiss). Surface projection of *GFP-LTi6b* signal
516 was generated by the software MerryProj [75], then rescaled and rotated (affine transformation)
517 to overlay the AFM image tiles. The resulting surface projection image was used to generate
518 cell contour image of the whole meristemic surface using morphological segmentation plugin
519 [76] for the software ImageJ (https://fiji.sc/), while the relative positions of each AFM
520 indentation location is then registered onto the cell contour image, along with cellular
521 geometrical and topological analyses, using the NanoIndentation plugin (version alpha) for
522 ImageJ [77].

523 Since each meristem had different turgor pressure range, cellular turgor pressure was
524 normalized to the average of each meristem for comparing cell-to-cell turgor pressure
525 heterogeneity without meristem-specific effects.

526 **Electron microscopy**

527 For serial block-face imaging SEM (SBF-SEM), plants were grown in vitro on medium
528 containing the auxin transport inhibitor NPA (Naphtalene Phtalamic Acid) to generate stems
529 with naked meristems and were locally treated for 48h with the microtubule depolymerizing
530 drug oryzalin (Sigma) in lanolin at a concentration of 2 µg/µl [78]. These plantlets were
531 subsequently taken off the inhibitor and left to regenerate for 48h on normal Arabidopsis
532 medium. Meristems with young organ primordia were fixed in 0.5% glutaraldehyde (in
533 demineralized water), from 25% Sigma stock in Microscopy Facility lab. The plantlets were

534 left at room temp for 2h in an eppendorf and rinsed 1x in water before post fixation and de-
535 hydrating and embedding in Spurr's epoxy as described in [79]. The samples were then
536 sectioned and viewed in a Zeiss Merlin SEM [79].

537 For standard transmission electron microscopy fixed meristems of soil grown plants were
538 embedded in Spurr's resin and sectioned before viewing in a Jeol 2100F (at the Centre
539 Technologique des Microstructures, UCBL, Lyon).

540 **Time-lapse confocal microscopy**

541 Untreated (dissected) and oryzalin-treated meristems were mounted and grown on ACM with
542 0.8% agarose and 0.1% PPM for live imaging. Confocal stacks were taken on an LSM 700
543 confocal microscope (Carl Zeiss) operated with the ZEN 2010 software (version 6.0, Carl
544 Zeiss), using a W N-Achroplan 40x/0.75 M27 water immersion objective, and on a TCS SP8
545 confocal microscope (Leica) operated with the Leica Application Suite X software (version 3.5,
546 Leica), using a Fluotar VISIR 25x/0.95 water immersion lens. GFP was excited at 488 nm and
547 emission detected between 415 – 735 nm. Stacks have resolution of 1028×1028 pixels, with
548 resolution ranging between 3.2 to 4.4 pixels/µm; Z steps were between 0.5 and 0.85µm.

549 For hyperosmotic treatments, meristems were mounted in Petri-dishes on Patafix (UHU), then
550 submerged in liquid ACM containing 0.1% PPM. Samples were first imaged in liquid ACM
551 (plus 0.1% PPM), then submersion medium was changed to ACM plus desired concentration
552 of NaCl (plus 0.1% PPM) by first rinsing with 3~5 mL target solution, then soaked in target
553 solution for 5 minutes before imaging. Because of the reduced signal in hyperosmotic solutions,
554 possibly due to the altered refractive index, stronger gain was used to reach comparable signal
555 intensity.

556 **Image processing and geometric analysis**

557 3D shell mesh and surface projection of untreated meristems were generated from confocal
558 stacks using the level set method (LSM) addon [80] for the software MorphoGraphX (MGX
559 version 1.0) [81]. For oryzalin-treated meristems, 2D surface projections were generated by
560 MerryProj [75] and imported into MGX for further processing. Projected images were

561 segmented using watershed method after manual seeding, and cell lineage between time points
562 was manually assigned in the meristem proper. To limit Z distortion and biases due to change
563 in inclination of the surface, which may affect analysis accuracy, only cells within 20° of
564 inclination angle from the highest position of the SAM were included. A custom-made Python
565 script was used to trace cell lineage between multiple time points and determine cell topology
566 based on the anticlinal wall number exported from MGX. Areal relative exponential growth
567 rate per hour was calculated as:

568 $$G = \frac{\ln(A_t/A_0)}{\Delta t}$$

569 where Δt is time interval in hours, A_0 is original cellular area at time t_0, and A_t is final area at
570 time $t_0 + \Delta t$. Cells undergone topological changes (i.e. divided cells and cells adjacent to new
571 division planes) during the acquisition were not included in the growth analyses. To analyse
572 variation, cell-specific growth rate was further co-aligning by the median per SAM then
573 stretching the distribution to the average first and third quartile positions to each data point.

574 To enhance the confocal images in hyperosmotic solution, anisotropic diffusion filter [82] was
575 re-implemented and applied to the raw images with the following parameters (specifications
576 see http://cbp-domu-forge.ens-lyon.fr/redmine/projects/anifilters/wiki): $K = 0.3$, $\sigma = 5$, $\gamma = 0.9$,
577 $D = 10$, 50 iterations.

578 For figure panels, brightness and contract of confocal images were linearly enhanced for better
579 visual. To synchronize panel shape and size, black background with no relevant information
580 was cropped from or added to the edge of the panels.

581 **Finite element method (FEM) indentation simulation**

582 Inflation and indentation simulations were performed with the same procedure adopted from
583 Mosca et al., 2017 [46]. For each meristem, a surface projection of the L1 anticlinal walls
584 obtained from confocal microscopy was segmented and extruded to the average anticlinal wall
585 height as observed in the template (5 µm for untreated and 10µm for oryzalin-treated) with the
586 CellMaker plugin for MorphoGraphX [81]. This generates a multicellular template made of
587 triangular membrane elements. The extruded meshes keep the average overall organ curvature.

In order to give the extruded cells a more realistic rest curvature (in the unpressurized state), both meshes were pre-inflated with a small pressure (0.05 MPa for untreated and 0.15 MPa oryzalin-treated SAM) and saved as the rest configuration. Both meshes were refined around the indentation points to increase the accuracy of the indentation simulations. The untreated mesh used in the indentation simulation and curvature analysis has an average edge size of 0.1 μm near the indentation points and increases to 0.5 μm far away from those points. The oryzalin-treated mesh has instead an average edge size of 0.2 μm and 1 μm near and far from the indentation the indentation areas, respectively.

The cell wall was modelled as a Saint-Venant Kirchhoff material represented by membrane elements with zero transversal stress and mathematically prescribed thickness [46]. The two templates were assigned the following material properties:

- isotropic material, 200 MPa Young's modulus, 0.3 Poisson ratio;

- cell wall thickness of 0.19 μm and 0.74 μm for the untreated and oryzalin-treated meristem, following experimental data.

The templates were inflated from the rest configuration with a turgor pressure of 2 MPa inside each cell for both meshes, until the forces equilibrium was reached (sum of the forces squared). With the chosen parameters, the total cell height after inflation is similar to the experimental observation from the confocal stacks for the referring templates (6.8 μm for untreated and 14.5 μm for oryzalin-treated). Afterwards the bottom of the template (bottom anticlinal cell walls) was blocked in all space degrees of freedom to simulate the presence of the supporting inner tissue during the indentation process.

The indentation is modelled as in [46] and is performed in the global z-direction as given by the confocal images. The indentation process is performed on each cell independently, where the specific indentation point is chosen to be close to the uppermost anticlinal wall location. This reproduces the AFM indentation modality. As in analysis of AFM experiments, the stiffness of the untreated cell was computed as the slope of the indentation curve at 0.5 μm indentation depth, with the reaction forces on the indenter between 0.3 and 0.7 μm depth used

for slope computation. For the oryzalin-treated, given the thicker walls, the indentations were deeper and the stiffness was computed around 1 μm indentation depth (reaction forces between 0.8 and 1.2 μm).

For both meshes, a refinement analysis was performed to verify the accuracy of the simulation results. The results are reported in Supplementary Table 1. We considered the variation of the coarse oryzalin mesh so small to justify using it for the AFM and curvature comparison analysis, while we preferred using the refined mesh for the untreated to reduce the error due to mesh resolution.

Mesh	coarse size	refined size	Relative MD	sd of relative MD
Untreated	0.2 μm	0.1 μm	3%	2.4%
Oryzalin-treated	0.4 μm	0.2 μm	2%	1.3%

Supplementary Table 1. FEM refinement analysis. Coarse mesh edge size near indentation; refined mesh average edge size near indentation; relative MD, relative mean absolute difference; sd, standard deviation.

Statistical analysis

Data were processed using Excel 2000 (Microsoft). All Tukey box plots depict the first, second (median) and third quartiles of data distribution, with whiskers marking the lowest/highest data within 1.5 interquartile ranges (IQR) of the lower/upper quartiles. Tukey's outliers are depicted as small circles outside the whiskers. Values like turgor pressure, cell area and growth rate were normalized to the average per meristem. After normalization, every cell was considered as one biological sample, and all linear regressions and Pearson correlations were performed on whole datasets. For simulations, cells on the edge of the mesh were not analysed due to border effect. Extremely rare polygon classes (i.e. triangle and nonagon) were not shown on the box plots in the main figures but were included in linear regression and Pearson correlation tests and were plotted in Figure S5. Kolmogorov–Smirnov test was used to distinguish cell neighbour number distribution (significance level $\alpha = 0.05$).

Mechanical-hydraulic modelling

Summary. We build a vertex-based model of plant tissues at cellular level that couples osmosis-driven hydraulic fluxes between cells and from apoplast with a fixed water potential, and cell wall mechanics which resists and grows under tension. Turgor and growth rate heterogeneities emerge from this coupling and from the heterogeneities in cells sizes and topology (number of neighbours).

We consider a collection of N polygonal cells $i = 1, \ldots, N$ that form a mesh; this mesh evolves with the appearance of new cells because of cell division. The walls between cells are discretized into one or several segments. Given the topology, the mesh is fully characterized by the position of the vertices. The walls are given a height h and a thickness w.

Cell wall rheology. The cell walls are modelled as a visco-elasto-plastic material, which would be equivalent to the Ortega model [20] in the case of an elongating cell. Let σ_k be the stress of a wall segment k; the constitutive law writes $\sigma_k = E_k \varepsilon_k^e$ where E_k is the elastic modulus and ε_k^e is the elastic deformation of the wall. Let l_k be the length of segment k, the rate of change of ε_k^e is given by:

$$\frac{\mathrm{d}\varepsilon_k^e}{\mathrm{d}t} + \Phi_k^w E_k \max\left(0, \varepsilon_k^e - \varepsilon_k^Y\right) = \frac{1}{l_k}\frac{\mathrm{d}l_k}{\mathrm{d}t}$$

where Φ_k^w is the extensibility and ε_k^Y is the yield deformation of segment k. Equivalently, we could define a yield stress.

Mechanical equilibrium. Let P_i be the turgor pressure in each cell i. The tissue being at every moment in a quasi-static equilibrium, pressure forces on wall edges and elastic forces within walls balance exactly at each vertex v:

$$\frac{1}{2}\sum_{k \in f(v)} \Delta_k P A_k \boldsymbol{n}_k + \sum_{k \in f(v)} E_k \varepsilon_k^e a_k \boldsymbol{e}_{k,v} = 0$$

Where $f(v)$ is the set of walls adjacent to junction v, and $\Delta_k P = P_{k_1} - P_{k_2}$ is the pressure jump across wall face k, with $k_1 < k_2$ as indices of the cells separated by face k, $A_k = h l_k$ is the area of the face k on which pressure is exerted, $\boldsymbol{n}_k$ is the normal vector to face k, oriented from cell k_1 to cell k_2, and $a_k = hw$ is the cross-section of the face, on which the elastic stress is exerted;

finally, $\boldsymbol{e}_{k,v}$ is the unit vector in the direction of face k, oriented from junction v to the other end of face k. In the case of a single cylindrical cell for which growth is restricted to its principal direction, the model is equivalent to the Lockhart-Ortega model.

Fluxes. For each cell i, the apoplasmic pathway is represented as a flux U_i^a (in volume per time unit) from the apoplast of constant water potential Ψ^a through a perfectly semi-permeable membrane: $U_i^a = A_i L_i^a (\Delta\Pi - P_i)$, where A_i is the area of each cell in contact with the apoplast, L_i^a is the corresponding water conductivity, $\Delta\Pi = \pi_i + \Psi^a$ is assumed constant, and π_i is the osmotic pressure of cell i.

The symplasmic pathway corresponds to flows that occur through plasmodesmata, channels between cells that convey both water and solutes. The symplasmic flows thus only depend on turgor pressure difference. Let L_{ij} be the symplasmic water conductivity corresponding to the interface between two neighbour cells i and j, and A_{ij} their contact area, both assumed symmetric: $L_{ij} = L_{ji}$ and $A_{ij} = A_{ji}$. The symplasmic flux U_{ji}^s (in volume per time unit) from cell j to i is defined by:

$$U_{ji}^s = A_{ij} L_{ij}^s \left(P_j - P_i\right)$$

Finally, the total water flux for cell i is the sum of the apoplasmic flux U_i^a and the symplasmic fluxes U_{ji}^s with all its neighbors, so that its volume variation can be expressed as:

$$\frac{\mathrm{d}V_i}{\mathrm{d}t} = A_i L_i^a (\Delta\Pi - P_i) + \sum_{j \in n(i)} A_{ij} L_{ij}^s \left(P_j - P_i\right)$$

where $n(i)$ is the set of neighbours of cell i.

Cell division. We implemented the Willis-Refahi rule [34], in which the division volume is given by $V_0 = f\, V_b + \mu_b (2 - f + Z)$, where $f = 0.5$, V_b is the volume at birth, $\mu_b = 3.31$ is the mean birth volume and Z is a Gaussian noise with zero mean and $\left(4\sigma_d^2 - f^2 \sigma_b^2\right)^{1/2}$ standard deviation, with $\sigma_b = 0.2$ and $\sigma_d = 0.1$.

Numerical resolution. In the Lockhart-Ortega model, the compatibility between wall elongation

and cell volume increase is automatically enforced through the geometrical constraint of unidirectional growth that leads to equal relative growth rate of the cell and strain rate of the walls. In our multicellular model, this equality is no longer true. Instead, the lengths $l(X)$ of the edges and the volumes $V(X)$ of the cells are expressed as functions of the positions X of the vertices; then, given an initial position X of the vertices and elastic deformation ε^e of the edges, the equations of wall rheology, mechanical equilibrium, and water fluxes form a closed set of equations with respect to the unknowns X, P, and ε^e that allow to predict their evolution.

To give an idea of the mathematical complexity of the problem, one may consider the following example: in a connected tissue, if one cell is stretched and forced to increase its volume, an equal volume of water has to enter the cell, either from the apoplastic compartment or the neighbour cells. In the latter case, pressure should drop in the neighbour cells, which should attract water from their own neighbours, and this could propagate to further cells depending on the geometry of the tissue and the effective parameters. Volume and therefore positions of the vertices could be also affected. Finally, one can see that the interaction between hydraulics and mechanics implies long range interactions where pressure plays a key role.

We developed an original algorithm and implemented it in an in-house code, where at each time step, the mechanical equilibrium is resolved under constraints on the cell volume (from the water fluxes), and constraints on the cells edges (from the rheological law of the walls). This was implemented in Python, using the open source libraries NumPy, SciPy, and the Topomesh class from the OpenAlea project (http://openalea.gforge.inria.fr/doc/vplants/container/doc/html/container/openalea_container_topomesh_ref.html). This algorithm is described in more detail in a separate publication [30].

The computations were run on a computer with a 3.6GHz Intel Xeon E5 processor, 64 GB of RAM, and running Linux Debian Stretch. The typical computing time was one week for each computation.

Parameterization of the model. The reference values of the parameters were chosen based on the literature or on our experiments (main text Table 1), except for α^s, for which no data is available and was conservatively ascribed an intermediate value of 0.5. Model behaviour was

explored by changing non-dimensional parameter values as explained in the main text.

Procedure for the computations. We first run in parallel three computations with cell division to around 300 cells. To mimic untreated case, simulations continue until around 600 cells. To mimic the oryzalin treatment, the current states of the "untreated" computations at around 300 cells are used as initial conditions for the oryzalin case: division is stopped, and we run computations either with the same effective parameters, or with some parameters modified so that the behaviour of the oryzalin treated meristems is recovered (see supplementary table 2); the computations are run until the total volume has been multiplied by three from this initial state. Typical runtime for one parameter set is one week.

Dividing simulations	SIM#	*n*	**Non-dividing simulations**	SIM#	*n*
Initial (Fig. 1f) $\alpha^s = 0.5$, $\alpha^a = 0.5$, $\theta = 7/3$	3	1535	No division (Fig. 1h, 6d)	3	759
Reference (Fig. 1g, 6a) $\alpha^s = 0.5$, $\alpha^a = 0.5$, $\theta = 20/3$	3	1496	$\Delta\Pi \times 2$	3	759
$\theta = 10 / 3$	3	1515	$w \times 2$	3	759
$\theta = 10$	3	1519	$w \times 4$ (Fig. 6g)	3	759
$\theta = 40 / 3$	3	1530	$\Delta\Pi \times 2$, $w \times 2$	3	759
$\alpha^s = 0.1$	3	1506	$\Delta\Pi \times 2$, $w \times 4$	3	759
$\alpha^s = 0.9$	3	1525			
$\alpha^a = 0.1$	3	1507			
$\alpha^a = 0.9$	3	1519			

Supplementary table 2. Parameter modification and simulation repeats. Parameters are systemically changed, with the reference parameter set $\alpha^s = 0.5$, $\alpha^a = 0.5$, $\theta = 20/3$ for exploration in untreated simulations and for mimicking oryzalin in non-dividing simulations. Annotations are as described above. SIM#, number of simulations; *n*, total cell number at last time point without boundary cells.

Acknowledgements

We thank P. Bolland and A. Lacroix for plant care, G. Cloarec for help with TEM, L. Beauzamy for AFM training, C. Mollier for help in estimating confocal technical errors, A. Kiss for help with anisotropic filtering parameterization, G. Cerutti for help in implementing the division algorithm and in segmentation, R. Smith for help in segmentation and mesh generation for the indentation simulations, and V. Battu, F. Zhao and C. Galvan-Ampudia for providing plant materials. We acknowledge the contribution of the PLATIM facility of SFR Biosciences (UMS3444/CNRS, US8/Inserm, ENS de Lyon, UCBL) for AFM and confocal microscopy, and of Centre Technologique des Microstructures (UCBL, Lyon) for electron microscopy. This work was supported by a fellowship from Institut Universitaire de France and an ERC Starting Grant "PhyMorph" to A.B. (ERC-2012-StG-307387), an EMBO Long-term Fellowship to Y.L. (EMBO ALTF 168-2015), and an Agropolis Foundation grant (MecaFruit3D) to I.C. and C.G.

Author contributions

This study was initiated by A.B. Y.L. and A.B. designed the experiments. Y.L. executed AFM and confocal microscopy, acquired experimental data except EM, and analysed experimental and simulation data. J.T. performed electron microscopy. V.M and M.D. wrote scripts to facilitate experimental data analysis. I.C. and C.G. designed physical model of tissue growth. I.C. implemented the model, ran simulations, optimized model parameters and analysed simulation data. G.M. designed, ran, and analysed indentation simulations. Y.L. and A.B. contributed to the design of simulations. Y.L., I.C., V.M., G.M., C.G. and A.B. contributed to data interpretation. Y.L. and A.B. wrote the manuscript with inputs from the other authors.

Data availability

All materials, scripts and datasets generated and analysed during the current study are available from the corresponding authors upon reasonable request.

754 **Figures**

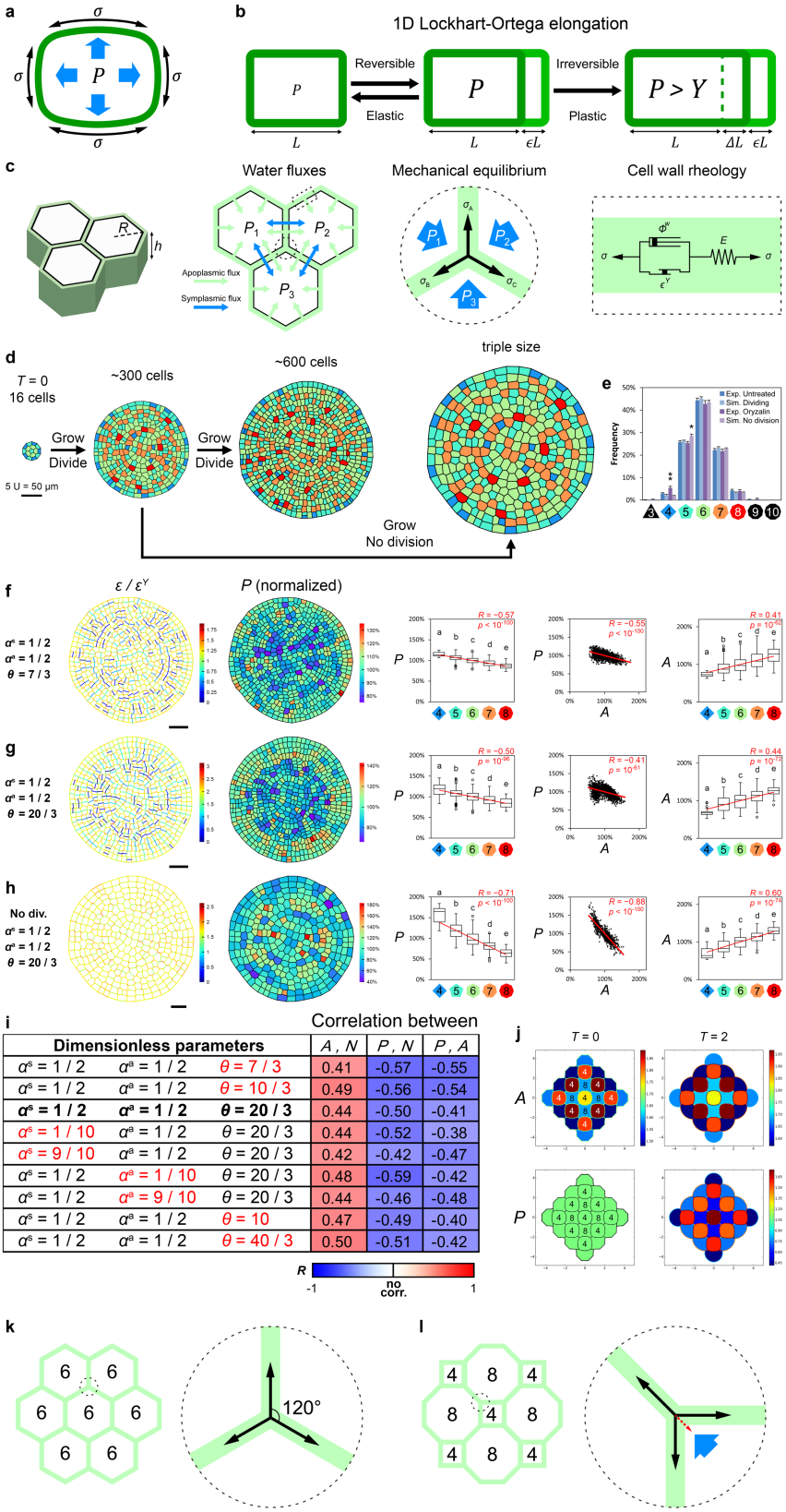

Dimensionless parameters			A , N	P , N	P , A
α^s = 1 / 2	α^a = 1 / 2	θ = 7 / 3	0.41	-0.57	-0.55
α^s = 1 / 2	α^a = 1 / 2	θ = 10 / 3	0.49	-0.56	-0.54
α^s = 1 / 2	**α^a = 1 / 2**	**θ = 20 / 3**	0.44	-0.50	-0.41
α^s = 1 / 10	α^a = 1 / 2	θ = 20 / 3	0.44	-0.52	-0.38
α^s = 9 / 10	α^a = 1 / 2	θ = 20 / 3	0.42	-0.42	-0.47
α^s = 1 / 2	α^a = 1 / 10	θ = 20 / 3	0.48	-0.59	-0.42
α^s = 1 / 2	α^a = 9 / 10	θ = 20 / 3	0.44	-0.46	-0.48
α^s = 1 / 2	α^a = 1 / 2	θ = 10	0.47	-0.49	-0.40
α^s = 1 / 2	α^a = 1 / 2	θ = 40 / 3	0.50	-0.51	-0.42

Figure 1. Turgor pressure heterogeneity emerges from cell topology in the mechano-hydraulic model.

(**a**) In a plant cell, the turgor pressure P is contained by the cell wall tensile stress σ. (**b**) A schematic representation of the Lockhart-Ortega equation, where 1D cell length L elongation is a combination of reversible stretch ϵL (elasticity, ϵ is elastic strain) and cell wall yield ΔL at longer timescale (viscosity) if P is higher than a threshold Y (effective plasticity, $\Delta L = \Phi t L (P - Y)$, Φ is wall extensibility, t is time). (**c**) Schematic representations of model components, including cell geometry with height h and radius R (left), apoplasmic/transmembrane and symplasmic/intercellular water fluxes (middle left), mechanical equilibrium at tricellular junctions (middle right) and the visco-elasto-plastic cell wall rheology (right). P_i, cell-specific turgor pressure; σ, cell wall tension; Φ^w, wall extensibility; ε^Y, wall strain threshold; E, wall Young's modulus. (**d**) Simulation snapshots: in "dividing" simulations, 16 initial cells grow and divide until about 600 cells; in "non-dividing" simulations, divisions are stopped when cell number reaches about 300 cells and growth continues until they triple in size. Colour indicates cell neighbour number as in (e). (**e**) Similar distributions of cell neighbour number in the experimentally observed (Exp.) shoot apical meristem and in simulations (Sim.) by Kolmogorov–Smirnov test (confidence level $\alpha = 0.05$, $D_{n,m} < D_\alpha$), error bars are standard deviations. *, Student's t-test $p < 0.05$; **, $p < 0.01$. (**f-h**) Cell wall strain, turgor pressure, neighbour number, and area in dividing (f, g) and non-dividing (h) simulations; the dimensionless parameter for flux-wall balance α^a, apoplasmic-symplasmic balance α^s and the osmotic drive are as indicated. Left: cell wall elastic strain ε normalized by yield strain ε^Y; middle left: cell turgor pressure P normalized by average pressure; middle: boxplots of normalized cellular turgor pressure P against cell topology N (**f**, n = 1535 cells; **g**, n = 1496 cells; **h**, n = 759 cells); middle right: normalized pressure against normalized area; right: normalized area against neighbour number. Cells on the mesh edge were not analysed due to border effect. Circles are Tukey's outliers; lowercase letters indicate statistically different populations (Student's t-test, $p < 0.05$); red lines indicate linear regressions, with Pearson correlation coefficient R and corresponding p-value. In (**d**, **f-h)** scale bars are 5 unit length. (**i**) Model parameter exploration. Colours indicate Person correlation coefficient R, with perfect anticorrelation as blue (R = -1), perfect correlation in red (R = 1); all correlations were statistically significant ($p < 0.05$). A, normalized cell area; N, cell neighbour number; P, normalized turgor pressure; α^a, dimensionless parameter for flux-wall balance; α^s, dimensionless parameter for apoplasmic-symplasmic balance; θ, dimensionless osmotic drive. (**j**) Simulations initiated with 4-edged bigger than 8-edged cells, shown at two simulation times, with area and pressure shown in top and bottom, respectively; 4-edged cells have higher pressure although bigger. (**k** to **l**) Schematic explanation of topology-derived turgor pressure heterogeneity. (**k**) Three-cell junctions in a tissue of hexagonal cells are at mechanical equilibrium with equal tensions and equal wall-wall angles. (**l**) Fewer-neighboured cells have sharper wall-wall angles, a tension that is roughly constant per wall effectively results in mechanical compression due to unequal projected tension distribution (red dash-line arrow) that is balanced by higher turgor pressure build-up (big blue arrow).

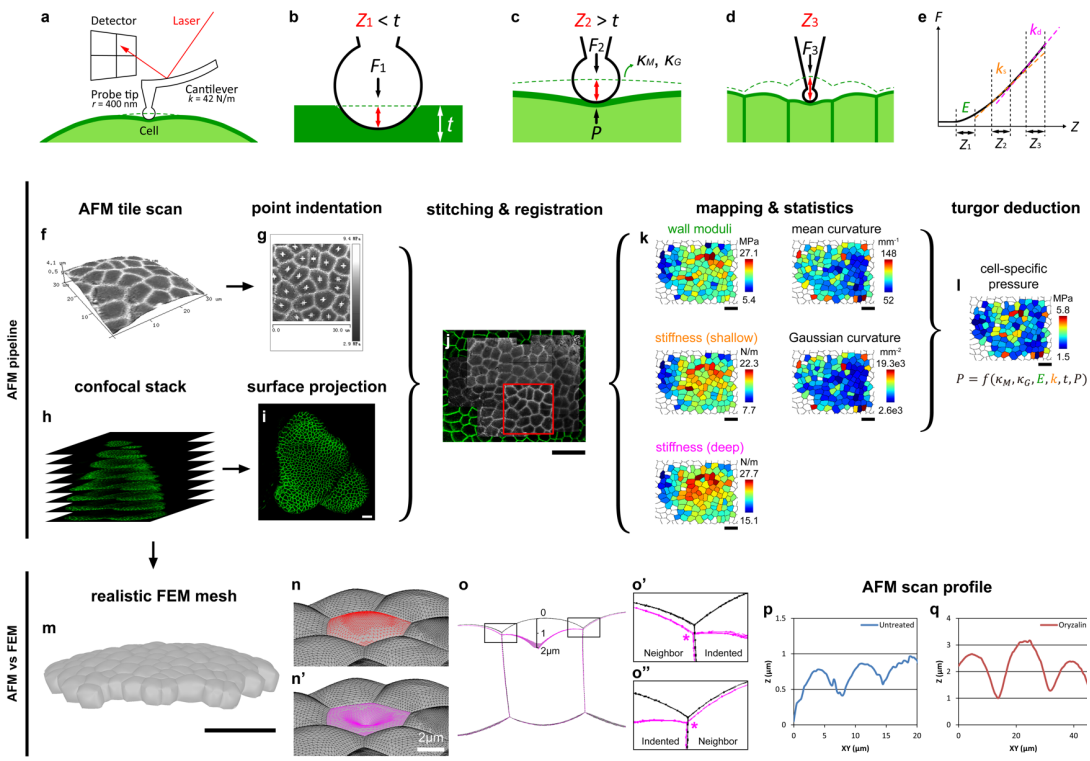

Figure 2. The experimental pipeline for turgor pressure deduction.

(**a**) Schematic representation of AFM nanoindentation for turgor pressure measurement. *r*, probe tip radius; *k*, cantilever stiffness. (**b** to **e**) Illustration for force curve interpretation at different indentation depth. (b) When indentation depth Z_1 is smaller than wall thickness *t*, the force-indentation curve is sensitive to cell wall property, (c) deeper-than-wall indentation $Z_2 > t$ is also sensitive to turgor pressure *P*. (d) Even deeper indentation Z_3 deforms surrounding cells and is also sensitive to tissue context. Dotted line marks the shell position before indentation, which is used to determine surface mean and Gaussian curvature, κ_M and κ_G, by AFM topographic scan. (e) Three regimes of the force-indentation curve are used to fit for cell wall Young's modulus *E*, apparent stiffness at cell-scale k_s and tissue scale k_d. *F* denotes indentation force. (**f** to **l**) The AFM-confocal pipeline of measurement and deduction on an example untreated SAM. (f) Derjaguin-Muller-Toporov (DMT) modulus map, highlighting cell contours, is projected on the surface topography of an AFM scan. Smaller scan region is chosen to bypass the SAM surface unevenness. (g) Multiple indentations (marked by crosshair) are performed near the barycentre of each cell. (h and i) Confocal stack and its surface projection of the same SAM with plasma membrane GFP signal. (j) Tiled AFM scans are overlaid and stitched on the confocal surface projection image, red square marking the same tile from (f and g). Individual indentation positions are registered on a global coordinate and assigned to segmented cells. (k) Force curves are analysed, and the cellular average of physical values are mapped. (l) Turgor pressure is deduced per force curve and averaged per cell. Stiffness from very deep indentation is not used for cell-specific deduction. (**m** to **o''**) Virtual indentation on realistic 3D mesh. (m) The epidermal layer is meshed based on confocal image. Cells are pressurized with a uniform 2 MPa turgor pressure. (n and n') A cell before (red) and being indented (magenta). (o to o'') Longitudinal section of the indented mesh; black, before indentation; magenta, being indented. Cell junctions

(rectangles) are magnified to highlight the neighbour cell deformation (marked by asterisks) by very deep indentation. (**p** and **q**) AFM-determined surface profiles of untreated (p) and oryzalin-treated SAM (q). Scale bars represent 20 µm if not specified. Note that z axes in (f, p and q) are stretched to emphasize SAM surface unevenness.

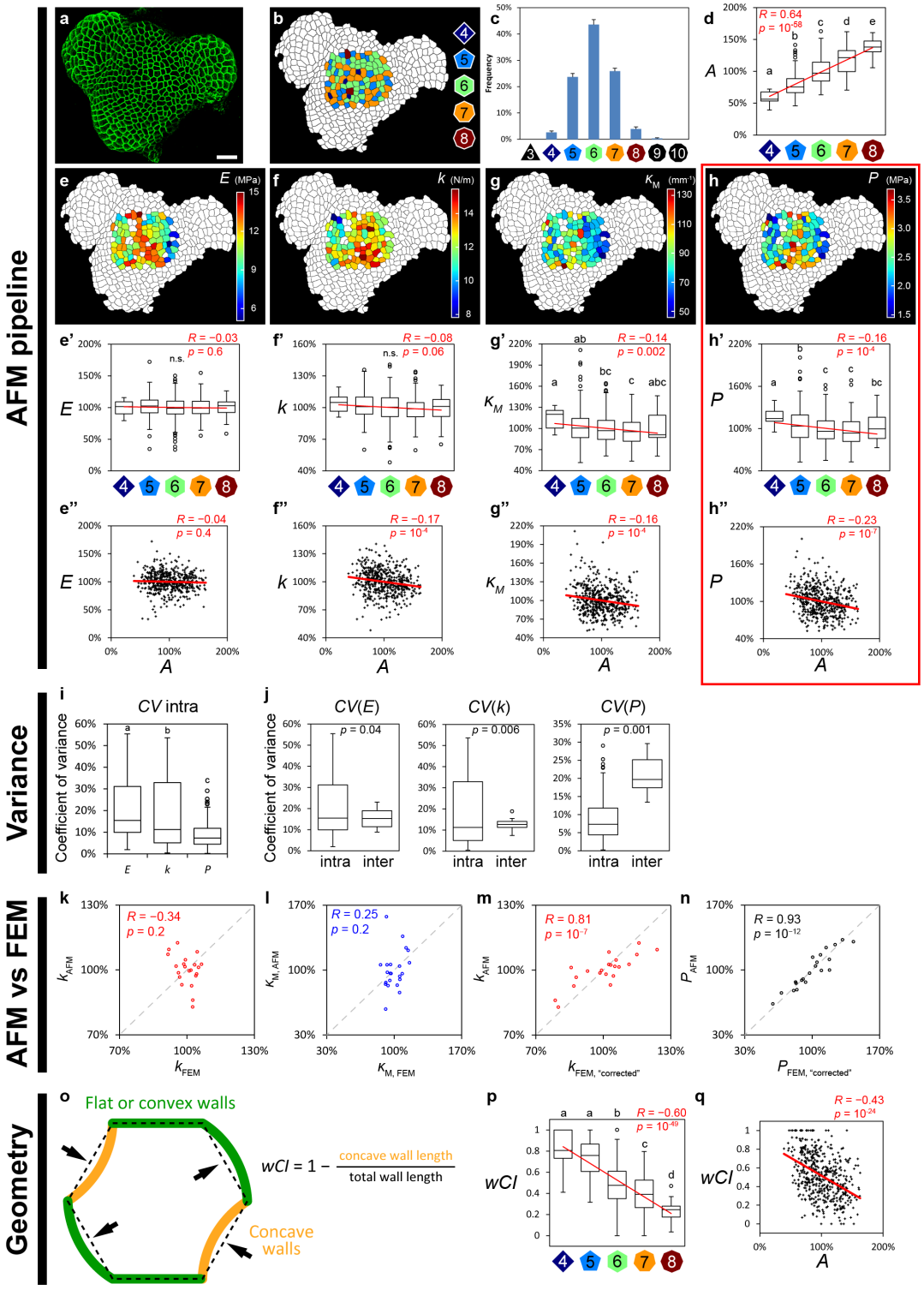

Figure 3. Turgor pressure heterogeneity in untreated SAM.

(**a**) Top-view surface projections of untreated SAM with plasma membrane GFP signal; scale bars represent 20 μm. (**b**) Map of epidermal cell neighbour number. (**c**) Distribution of neighbour number on 7 untreated SAM surfaces, error bars are standard errors of means. (**d**) Normalized cell area A and cell neighbour number N are linearly correlated. (**e** to **h''**) AFM-determined cellular values and their association with neighbour number N and cell area A, all plotted values are normalized per SAM (7 SAMs, n = 503 cells). (e to e'') Cell wall Young's moduli E, (f to f'') apparent stiffness k at intermediate indentation depth, (g to g'') cell surface mean curvature κ_M, (h to h'') deduced turgor pressure P. (**i** and **j**) Coefficient of variance (CV) of AFM-determined values in untreated meristems. (i) At subcellular scale (intra), P is much less variable than E and k. (j) P, unlike E and k, are more heterogeneous between cells (inter) than between measurements within single cells (intra). (**o** to **q**) Weighed convex index (wCI) anticorrelates with cell neighbour number (p) and normalized cell area (q). In box plots, circles are Tukey's outliers; lowercase letters indicate statistically different populations (Student's t-test, $p < 0.05$); red lines indicate linear regressions, with Pearson correlation coefficient R and corresponding p-value.

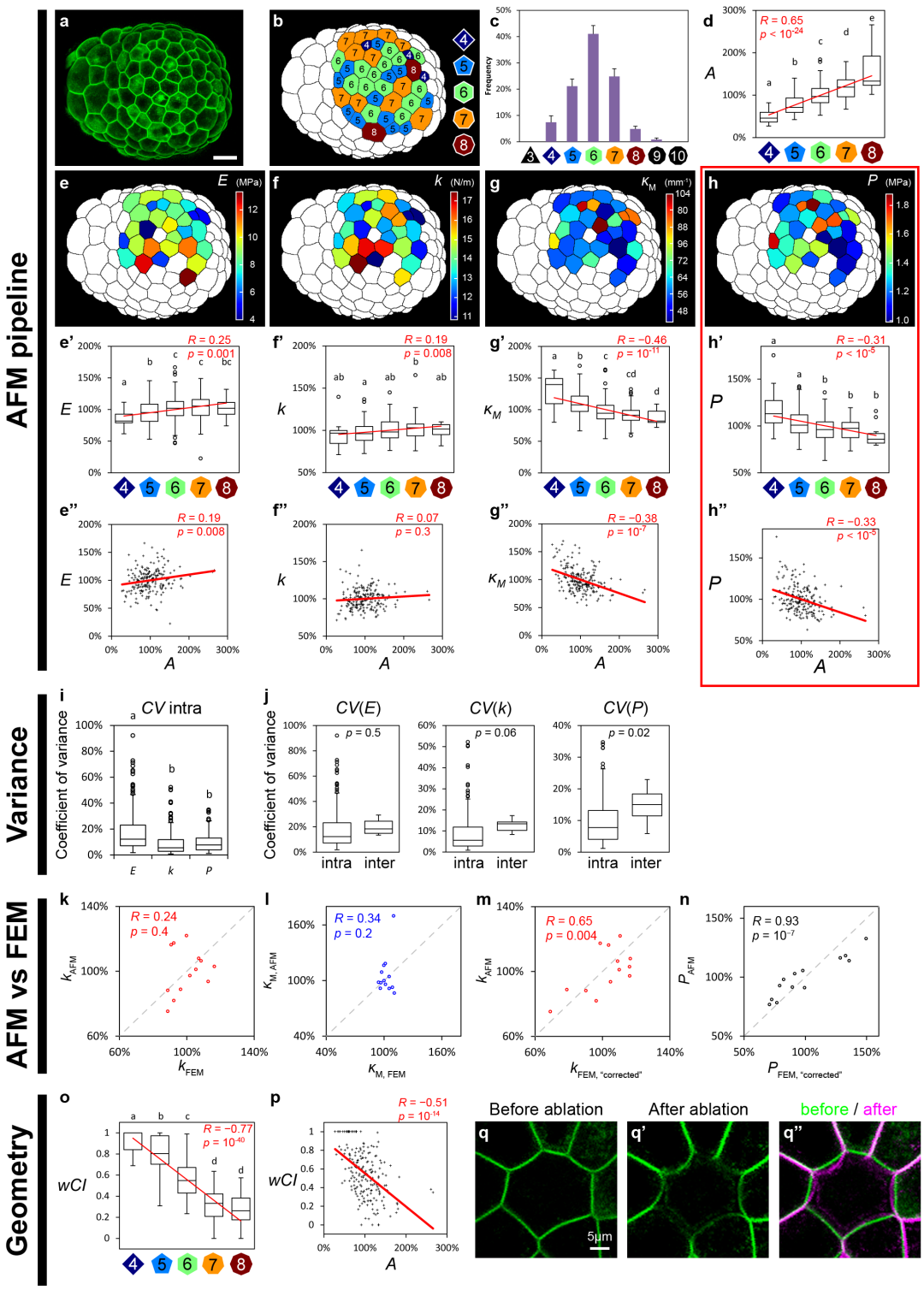

Figure 4. Turgor pressure heterogeneity in oryzalin-treated SAM.
(**c**) Top-view surface projections of oryzalin SAM with plasma membrane GFP signal; scale bars represent 20 µm. (**b**) Map of epidermal cell neighbour number. (**c**) Distribution of neighbour number on 9 untreated SAM surfaces, error bars are standard errors of means. (**d**) Normalized cell area *A* and cell neighbour number *N* are linearly correlated. (**e** to **h”**) AFM-determined cellular values and their association with neighbour number *N* and cell area *A*, all plotted values are normalized per SAM (9 SAMs, *n* = 202 cells). (e to e”) Cell wall

Young's moduli E, (f to f'') apparent stiffness k at intermediate indentation depth, (g to g'') cell surface mean curvature κ_M, (h to h'') deduced turgor pressure P. (**i** and **j**) Coefficient of variance (CV) of AFM-determined values in untreated meristems. (i) At subcellular scale (intra), P and k are much less variable than E. (j) P and k, unlike E, are more heterogeneous between cells (inter) than between measurements within single cells (intra). (**o** to **q''**) Weighed convex index (wCI) anticorrelates with cell neighbour number (o) and normalized cell area (p). (q to q'') Cell walls curve towards cell with low pressure, as signified by the enhanced curvature towards the ablated cell with released pressure. In box plots, circles are Tukey's outliers; lowercase letters indicate statistically different populations (Student's t-test, $p < 0.05$); red lines indicate linear regressions, with Pearson correlation coefficient R and corresponding p-value.

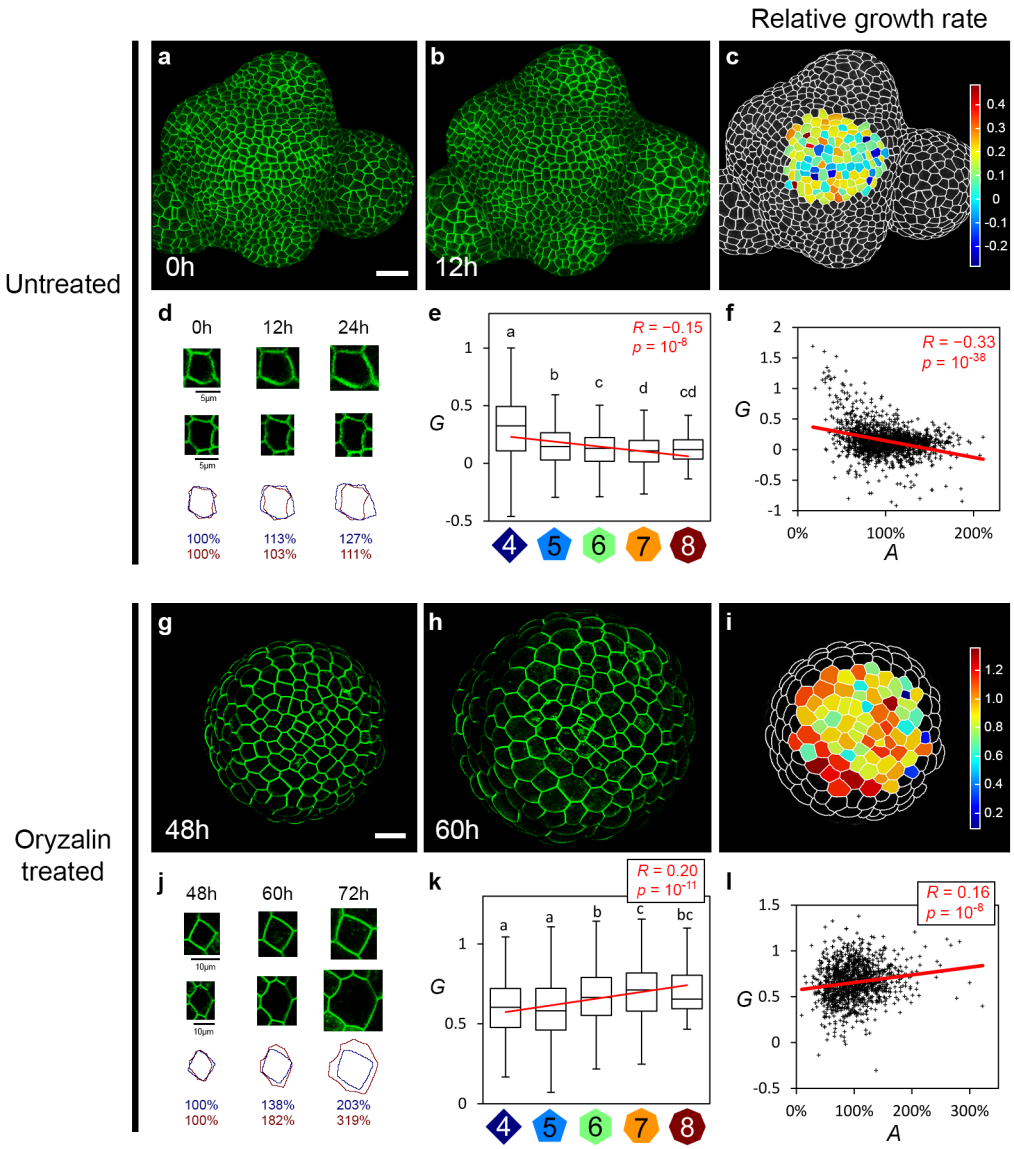

Figure 5. Cellular growth rate bifurcates between conditions.
(**a** to **f**) Relative growth rate per day G of untreated SAM cells. (**g** to **l**) Cellular growth rate per day of oryzalin-treated SAM between 12-hour interval (48 and 60 hours post treatment). (a, b, g and h) Surface projections of untreated or oryzalin-treated SAM at initial time point

(a and g) and 12 hours later (b and h); scale bars are 20 μm unless otherwise noted. (c and i) Heat maps of areal relative growth rate per day. (d and j) Example 4 and 8-neighbored cells during 24-hour growth, with areal normalization at initial time point. Cell contour and relative size (blue for 4-neighbored, red for 8-neighbored) depict the diverging growth trends. Scale bars are as indicated. (e, f, k and l) Box plots of relative growth rate per day G against cell topology N (e and k) and dot plots of relative growth rate per day G against normalized cell area A (f and l) (e and f, untreated 11 SAMs, n = 1491 cells; k and l, oryzalin-treated 14 SAMs, n = 1160 cells). Note that Tukey's outliers are plotted in Figure S5 and all data are included for statistical analyses. Lowercase letters indicate statistically different populations (Student's t-test, $p < 0.05$); red lines indicate linear regressions, with Pearson correlation coefficient R and corresponding p-value.

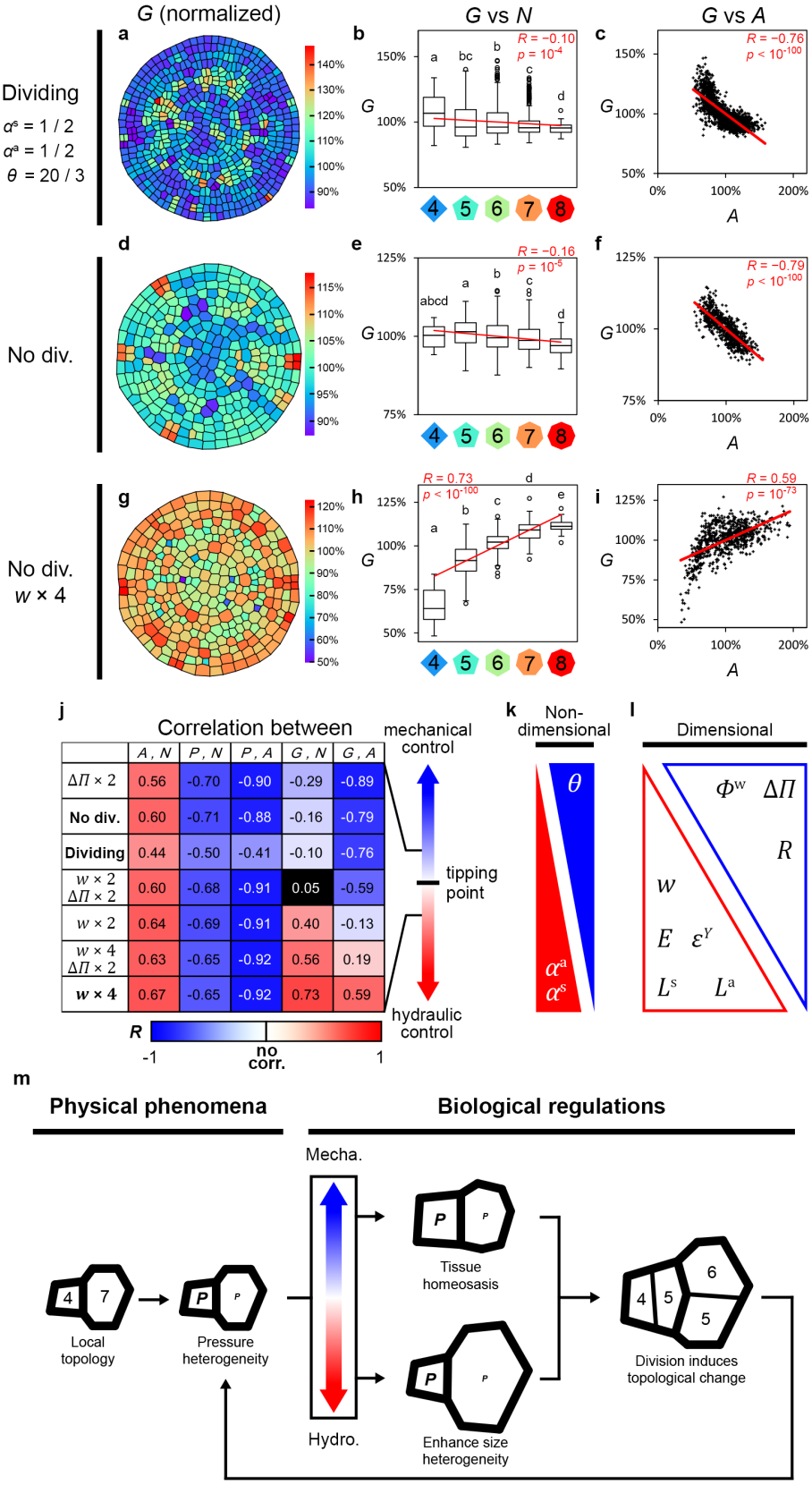

Figure 6. The model recapitulates the untreated and oryzalin-treated growth trends. (**a** to **i**) Relative growth rate G normalized by average growth rate, neighbour number N, and normalized cell area A, with reference values of dimensionless parameters ($\alpha^a = 0.5$, $\alpha^s = 0.5$,

θ = 20/3): dividing simulations (a-c), non-dividing simulations (d-f), and non-dividing simulations with quadruple wall thickness w to mimic oryzalin treatment (g-i). (a, d, g) Heat maps of normalized areal relative growth rate. (b, e, h) Box plots of normalized relative growth rate G against cell topology N. Lowercase letters indicate statistically different populations (Student's t-test, $p < 0.05$); red lines indicate linear regressions, with Pearson correlation coefficient R and corresponding p-value. (c, f, i) Dot plots of normalized relative growth rate G against normalized cell area A. For numbers of repeats see STAR Methods. (**j**) Model exploration to fit oryzalin-treated case. Colours indicate Person correlation R, with perfect anticorrelation as blue (R = -1), perfect correlation in red (R = 1), and insignificant correlation ($p > 0.05$) in black. A, normalized cell area; N, cell neighbour number; P, normalized turgor pressure; G, normalized relative growth rate; $\Delta\Pi$, transmembrane osmotic pressure difference; w, wall thickness. (**k, l**) Influence of dimensionless (k) and dimensional parameters (l) on growth trends. Triangles indicate parameter's influence to the mechanical–hydraulic balance. α^{a}, dimensionless parameter for flux-wall balance; α^{s}, dimensionless parameter for symplasmic-apoplasmic balance; θ, dimensionless osmotic drive. w, wall thickness; E, cell wall modulus; ε^{Y}, strain threshold; L^{a}, cross-membrane water conductivity; L^{s}, cell-to-cell symplasmic conductivity; Φ^{w}, wall extensibility; $\Delta\Pi$, transmembrane osmotic pressure difference; R, representative cell size. (**m**) Summary of growth trend inversion according to the mechanical–hydraulic control shown in (j). The wall and flux limits correspond to untreated and oryzalin-treated SAMs, respectively.

Supplementary figures

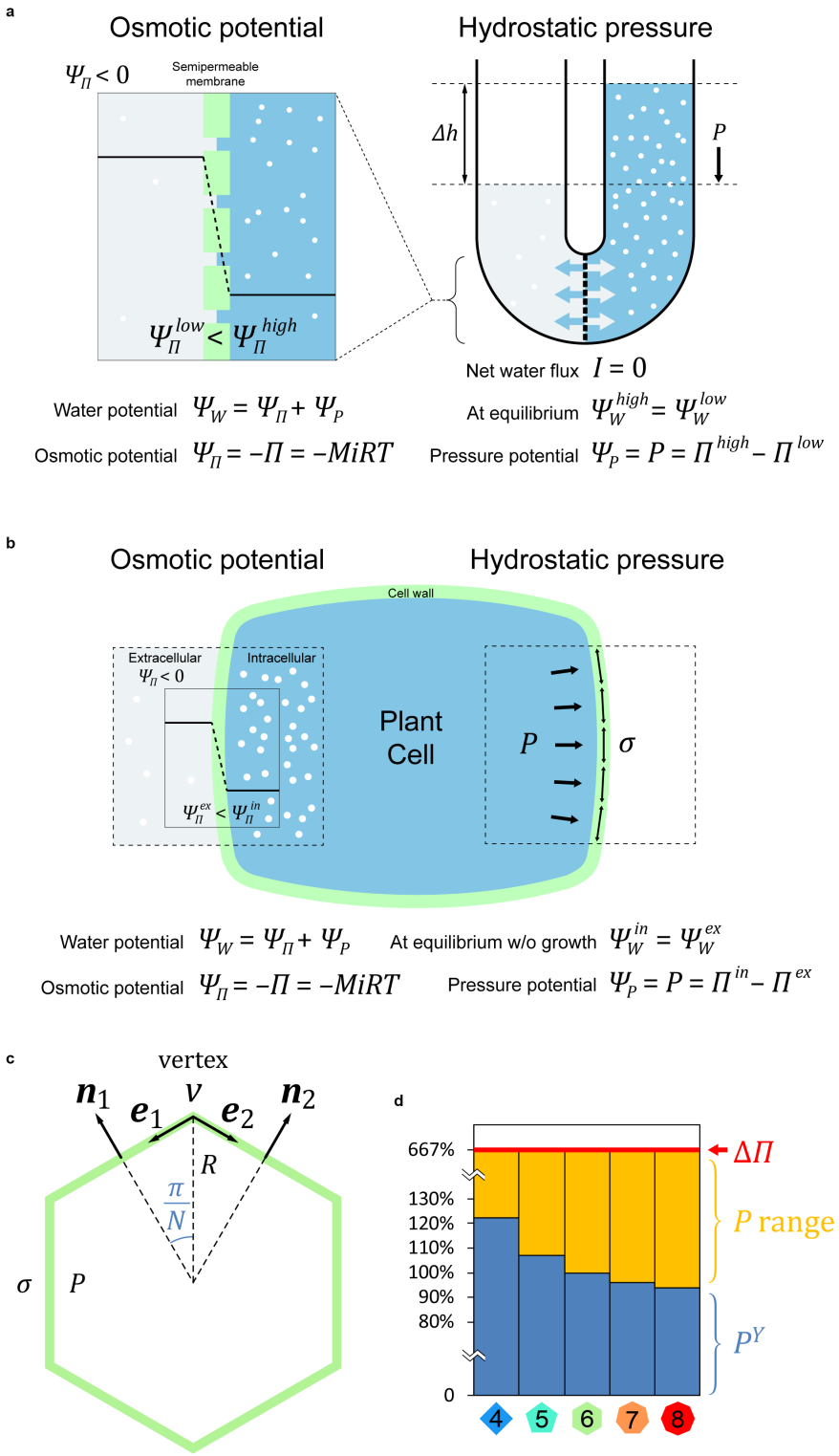

Figure S1. Osmotic pressure and hydrostatic pressure.
(**a**) Osmosis occurs when solutions of different osmotic pressure Π, due to different solute concentration (depicted by the density of white dots), are separated by a semipermeable membrane. Difference of osmotic potential Ψ_Π (depicted by horizontal black lines, always negative in solutions) across the membrane dictates that solvent flows from high to low

potential compartment (low to high solute concentration). In a U-shaped tube setup (right), osmosis may stop before the two compartments reach the same concentration, as the extra volume (in fact height, Δh) in the higher-concentration compartment exerts a hydrostatic pressure P due to gravity that pushes the solvent back. P increases until reaching the same value as $\Delta\Pi$ at equilibrium where the total water potential Ψ_W is equal on both sides, and the net solvent flux $I = 0$ (indicated by the opposite blue arrows). M, solute molar concentration; i, van t'Hoff index of solute that disassociates; R, ideal gas constant; T, absolute temperature. (**b**) Osmosis in a plant cell, where gravity is neglected for its small size. Because of the rigid cell wall that restricts the cell volume, hydrostatic pressure P, alias turgor pressure, builds up alongside cell wall tension σ to counterbalance the difference of osmotic potential Ψ_Π, until $P = \Delta\Pi$. (**c**) Geometrical extension of Lockhart model for a single polygonal cell. σ, cell wall stress; P, turgor pressure; R, cell radius; N, polygon class; v, vertex; $\boldsymbol{n_1}$ and $\boldsymbol{n_2}$; normal vector; $\boldsymbol{e_1}$ and $\boldsymbol{e_2}$, tangent vector. (**d**) Half of the threshold pressure of a polygonal cells base on $P^Y = \frac{w}{2R\cos(\pi/N)} E\varepsilon^Y$. For growing cells, turgor pressure P falls between the transmembrane osmotic pressure $\Delta\Pi$ and pressure threshold P^Y.

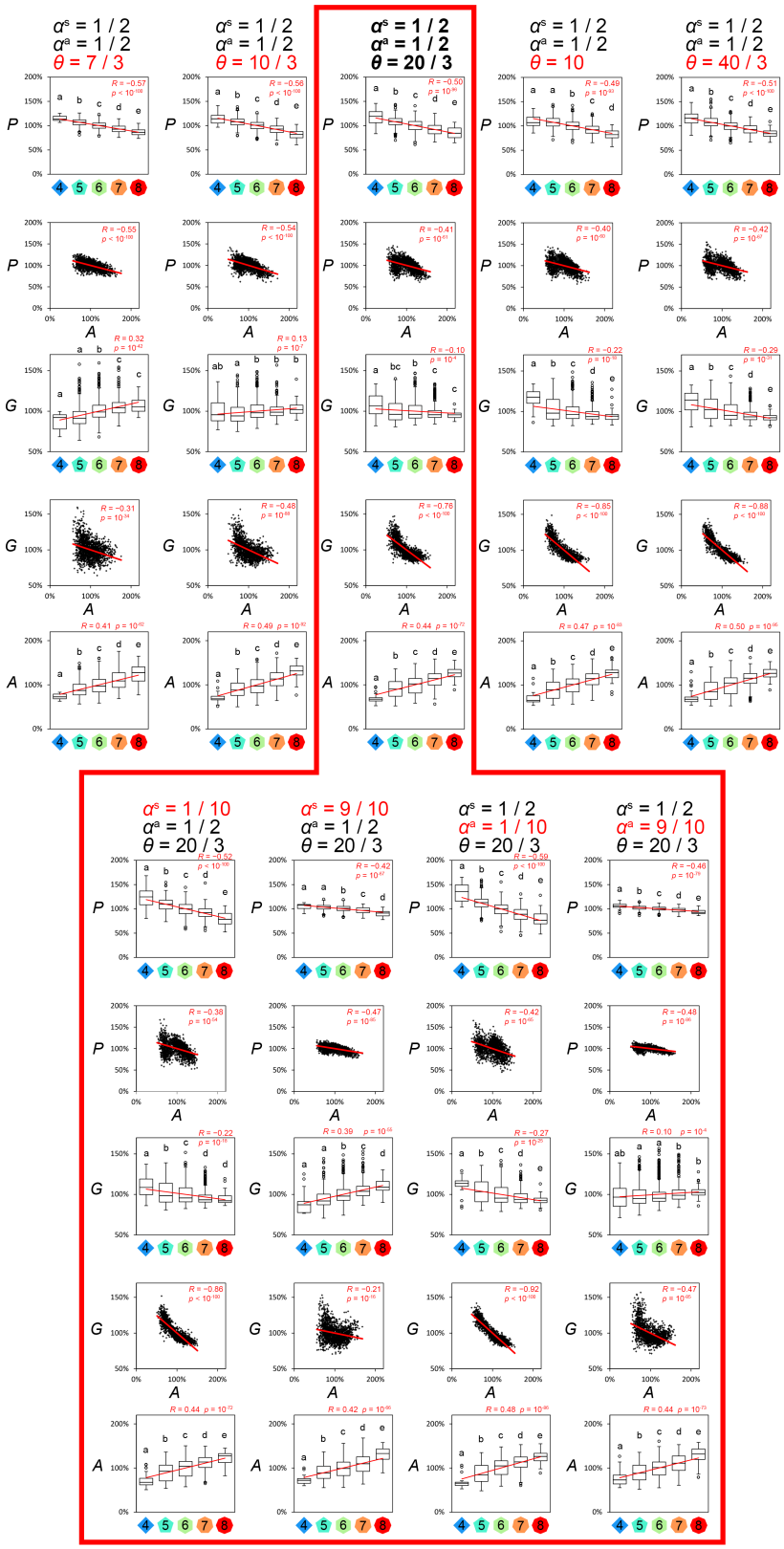

Figure S2. Simulations for vertex model parameter exploration.

Model parameters were systemically changed. α_a, dimensionless parameter determining the weight of the limitation of growth by transmembrane permeability to the combined limitation of growth by cell wall extensibility and transmembrane permeability; α_s, dimensionless

parameter determining the weight of intercellular water conductivity over total (intercellular and transmembrane) conductivity; *s*, cell size scale at division relative to the initial setting. *P*, normalized turgor pressure, *A*, normalized cell area; *G*, relative growth rate per hour. Polygons indicate cell neighbour number. Red lines indicate linear regressions, with Pearson correlation coefficient *R* and corresponding *p*-value.

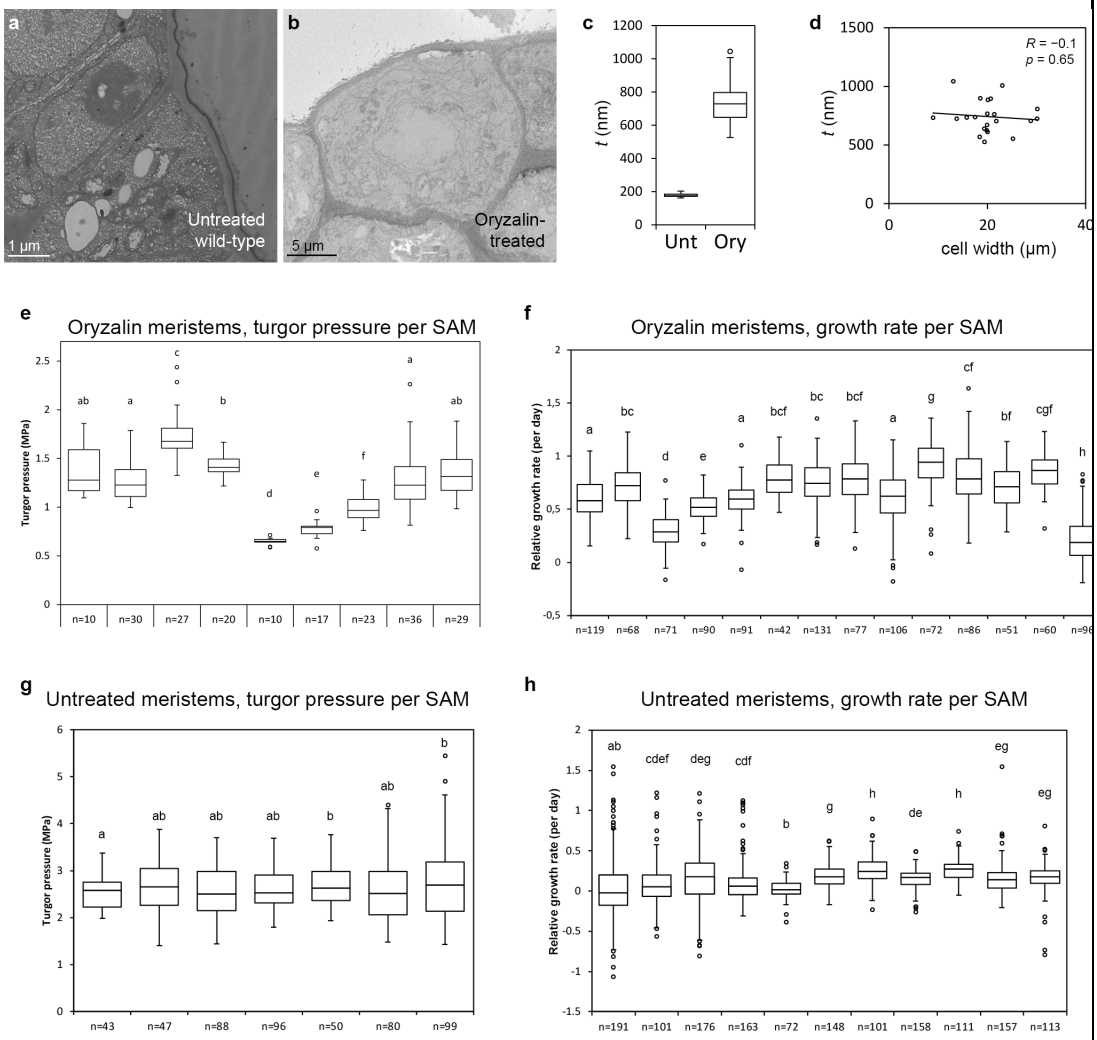

Figure S3. Cell wall thickness and individual SAM measurements of turgor pressure and growth rate.

(**a** and **b**) TEM and serial block-face imaging SEM images of untreated (a) and oryzalin-treated meristem (b). (**c**) Boxplots of surface wall thickness of untreated (Unt) and oryzalin-treated (Ory) meristems. (**d**) Surface wall thickness does not correlate to cell width in oryzalin-treated meristems. (**e-h**) Oryzalin-treated SAMs showed highly variable turgor pressure and growth rate per SAM, while untreated samples show little variation; *n* is cell number measured per meristem. Circles are Tukey's outliers; lowercase letters indicate statistically different populations (Student's *t*-test, $p < 0.05$). (g) The first five untreated meristems measured by AFM were of ecotype WS-4, while the last two are of Col-0.

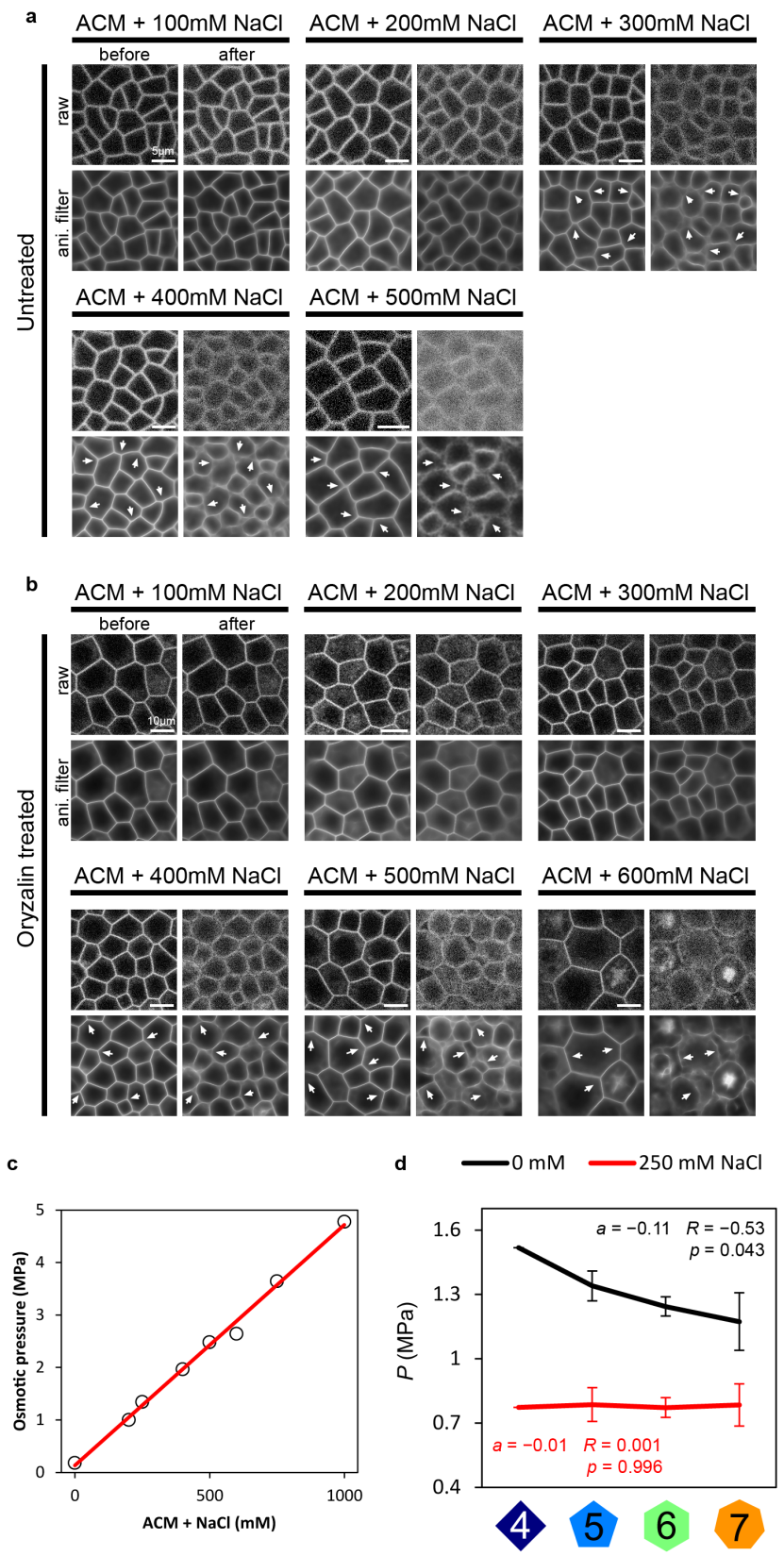

Figure S4. Hyperosmotic treatments on SAMs.

(**a** and **b**) Confocal images of untreated (a) and oryzalin-treated (b) meristems submerged in liquid apex culture medium (ACM) before and after the supplementation of NaCl. The

increased osmolality resulted in blurred images (each upper-right subpanel), possibly due to altered refraction limit, which required anisotropic filtering to enhance the trajectory of cell contours. Out of 8 untreated meristems, half showed incipient plasmolsysis at 200 mM NaCl (~0.4 Osm) and the other half at 300 mM (~0.6 Osm). For 7 oryzalin-treated meristems, incipient plasmolysis occurred among a broader osmolarity (2 meristems at 300 mM, 3 meristems at 400 mM, 2 meristems at 500 mM). Arrows points to noticeable membrane detachment and rounding, indicating plasmolysis. (**c**) Osmolarity calibration by osmometer measurements ($r^2 > 0.99$). (**d**) Moderate hyperosmotic treatment decreases AFM-determined turgor pressure, and reduces turgor heterogeneity plotted against cell neighbour number (linear regression slope *a*, Pearson correlation coefficient *R* and corresponding *p*-value).

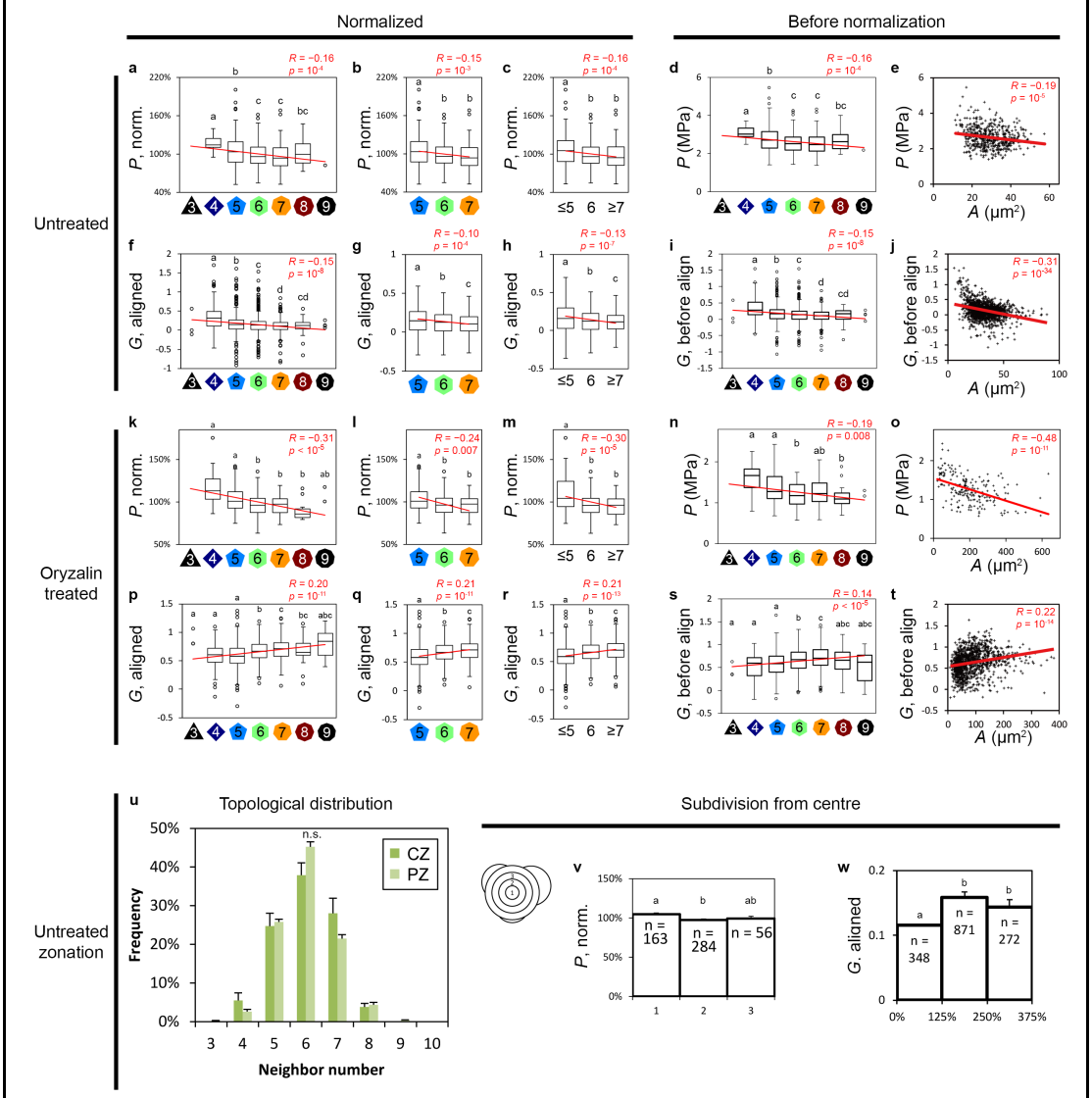

Figure S5. Pressure and growth rate before and after normalization, and regional measurements.

(**a** to **j**) Normalized and raw turgor pressure *P* and growth rate *G* of untreated meristems plotted against cell neighbour number *N* and cell area *A*. (**k** to **t**) Normalized and raw turgor pressure *P* and growth rate *G* of oryzalin-treated meristems plotted against cell neighbour number and cell area. (a, f, k, p) Normalized *P* and co-aligned *G* against *N* plots complete

with outliers and the rare 3- and 9-neighboured cells, same data as in Figure 3 and 4. (b, g, l, q) Same normalized data with only the major polygonal classes (N = 5, 6, 7), showing that the correlations do not depend on the rare polygonal classes at the ends of distributions. (c, h, m, r) Same normalized data were binned for cells with 5 or fewer neighbours (≤5), cells with 6 neighbours and cells with 7 or more neighbours (≥7), showing the same trends as unbinned data. (d, i, n, s) Raw data of P and G before normalization / co-alignment against neighbour number; (e, j, o, t) raw data of P and G before normalization / co-alignment against unnormalized cell area, all showing the same trend as normalized data. Red lines are linear regression line, with Pearson correlation coefficient R and corresponding p-value. Lower case letters denote statistically significant groups (Student's t-test $p < 0.05$). (**u**) Frequency of N-neighboured cells in central zone (CZ) and peripheral zone (PZ) shows no significant difference (Kolmogorov–Smirnov test, confidence level $\alpha = 0.05$, $D_{n,m} < D_\alpha$). (**v, w**) Normalized turgor pressure and co-aligned growth rate in subregions of SAM; n is cell number, error bars indicate standard error of mean, lower case letters denote statistically significant groups (Student's t-test $p < 0.05$).

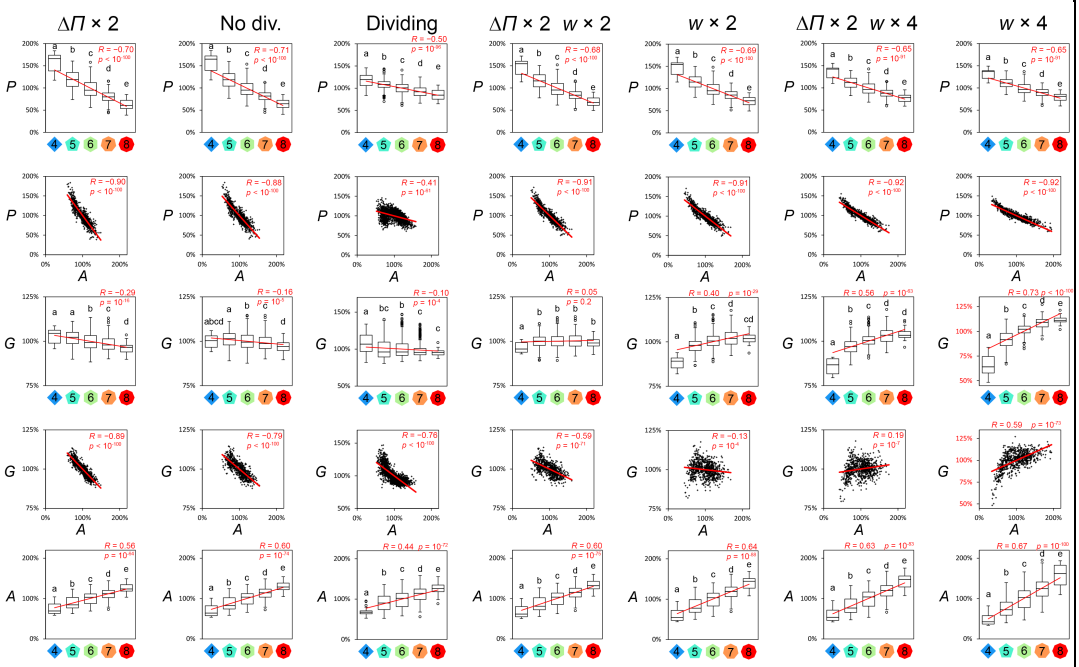

Figure S6. Simulations to recapitulate oryzalin-treated SAM.
Based on the reference parameter set ($\alpha^s = 0.5$, $\alpha^a = 0.5$, $\theta = 20/3$), which represents the untreated-like behaviour with cell divisions (Dividing), oryzalin-treated-like behaviour was further fitted by stopping cell division (No div.) and subsequently changing osmotic pressure $\Delta\Pi$ and cell wall thickness w, based on experimental observations. P, normalized turgor pressure, A, normalized cell area; G, normalized relative growth rate. Polygons indicate cell neighbour number. Red lines indicate linear regressions, with Pearson correlation coefficient R and corresponding p-value.

757

References

1. Hong, L.; Dumond, M.; Zhu, M.; Tsugawa, S.; Li, C.-B.; Boudaoud, A.; Hamant, O.; Roeder, A.H.K. Heterogeneity and Robustness in Plant Morphogenesis: From Cells to Organs. *Annu. Rev. Plant Biol.* **2018**, *69*, 469–495.
2. Kamimoto, K.; Kaneko, K.; Kok, C.Y.-Y.; Okada, H.; Miyajima, A.; Itoh, T. Heterogeneity and stochastic growth regulation of biliary epithelial cells dictate dynamic epithelial tissue remodeling. *eLife* **2016**, *5*.
3. Ietswaart, R.; Rosa, S.; Wu, Z.; Dean, C.; Howard, M. Cell-Size-Dependent Transcription of FLC and Its Antisense Long Non-coding RNA COOLAIR Explain Cell-to-Cell Expression Variation. *Cell Syst.* **2017**, *4*, 622-635.e9.
4. Long, Y.; Stahl, Y.; Weidtkamp-Peters, S.; Postma, M.; Zhou, W.; Goedhart, J.; Sánchez-Pérez, M.-I.; Gadella, T.W.J.; Simon, R.; Scheres, B.; et al. In vivo FRET-FLIM reveals cell-type-specific protein interactions in Arabidopsis roots. *Nature* **2017**, *548*, 97–102.
5. Chubb, J.R. Symmetry breaking in development and stochastic gene expression. *Wiley Interdiscip. Rev. Dev. Biol.* **2017**, *6*, e284.
6. Donati, G.; Watt, F.M. Stem Cell Heterogeneity and Plasticity in Epithelia. *Cell Stem Cell* **2015**, *16*, 465–476.
7. Gerdes, M.J.; Sood, A.; Sevinsky, C.; Pris, A.D.; Zavodszky, M.I.; Ginty, F. Emerging Understanding of Multiscale Tumor Heterogeneity. *Front. Oncol.* **2014**, *4*.
8. Eldar, A.; Elowitz, M.B. Functional roles for noise in genetic circuits. *Nature* **2010**, *467*, 167–173.
9. Watanabe, K.; Umeda, T.; Niwa, K.; Naguro, I.; Ichijo, H. A PP6-ASK3 Module Coordinates the Bidirectional Cell Volume Regulation under Osmotic Stress. *Cell Rep.* **2018**, *22*, 2809–2817.
10. Xie, K.; Yang, Y.; Jiang, H. Controlling Cellular Volume via Mechanical and Physical Properties of Substrate. *Biophys. J.* **2018**, *114*, 675–687.
11. Guo, M.; Pegoraro, A.F.; Mao, A.; Zhou, E.H.; Arany, P.R.; Han, Y.; Burnette, D.T.; Jensen, M.H.; Kasza, K.E.; Moore, J.R.; et al. Cell volume change through water efflux impacts cell stiffness and stem cell fate. *Proc. Natl. Acad. Sci.* **2017**, *114*, E8618–E8627.
12. Dumais, J.; Forterre, Y. "Vegetable Dynamicks": The Role of Water in Plant Movements. *Annu. Rev. Fluid Mech.* **2012**, *44*, 453–478.
13. Stewart, M.P.; Helenius, J.; Toyoda, Y.; Ramanathan, S.P.; Muller, D.J.; Hyman, A.A. Hydrostatic pressure and the actomyosin cortex drive mitotic cell rounding. *Nature* **2011**, *469*, 226–230.
14. Montel, F.; Delarue, M.; Elgeti, J.; Malaquin, L.; Basan, M.; Risler, T.; Cabane, B.; Vignjevic, D.; Prost, J.; Cappello, G.; et al. Stress clamp experiments on multicellular tumor spheroids. *Phys. Rev. Lett.* **2011**, *107*, 188102.
15. Rojas, E.R.; Huang, K.C. Regulation of microbial growth by turgor pressure. *Curr. Opin. Microbiol.* **2017**, *42*, 62–70.
16. Zerzour, R.; Kroeger, J.; Geitmann, A. Polar growth in pollen tubes is associated with spatially confined dynamic changes in cell mechanical properties. *Dev. Biol.* **2009**, *334*, 437–446.
17. Lopez, R.; Badel, E.; Peraudeau, S.; Leblanc-Fournier, N.; Beaujard, F.; Julien, J.-L.; Cochard, H.; Moulia, B. Tree shoot bending generates hydraulic pressure pulses: a new long-distance signal? *J. Exp. Bot.* **2014**, *65*, 1997–2008.
18. Beauzamy, L.; Nakayama, N.; Boudaoud, A. Flowers under pressure: ins and outs of turgor

regulation in development. *Ann. Bot.* **2014**, mcu187.
19. Feng, W.; Lindner, H.; Robbins, N.E.; Dinneny, J.R. Growing Out of Stress: The Role of Cell- and Organ-Scale Growth Control in Plant Water-Stress Responses. *Plant Cell* **2016**, *28*, 1769–1782.
20. Ortega, J.K. Augmented growth equation for cell wall expansion. *Plant Physiol.* **1985**, *79*, 318–320.
21. Kroeger, J.H.; Zerzour, R.; Geitmann, A. Regulator or driving force? The role of turgor pressure in oscillatory plant cell growth. *PloS One* **2011**, *6*, e18549.
22. Sager, R.E.; Lee, J.-Y. Plasmodesmata at a glance. *J. Cell Sci.* **2018**, *131*, jcs209346.
23. Willmer, C.M.; Sexton, R. Stomata and plasmodesmata. *Protoplasma* **1979**, *100*, 113–124.
24. Wille, A.C.; Lucas, W.J. Ultrastructural and histochemical studies on guard cells. *Planta* **1984**, *160*, 129–142.
25. Ruan, Y.L.; Llewellyn, D.J.; Furbank, R.T. The control of single-celled cotton fiber elongation by developmentally reversible gating of plasmodesmata and coordinated expression of sucrose and K+ transporters and expansin. *Plant Cell* **2001**, *13*, 47–60.
26. Rygol, J.; Pritchard, J.; Zhu, J.J.; Tomos, A.D.; Zimmermann, U. Transpiration Induces Radial Turgor Pressure Gradients in Wheat and Maize Roots. *Plant Physiol.* **1993**, *103*, 493–500.
27. Robbins, N.E.; Dinneny, J.R. Growth is required for perception of water availability to pattern root branches in plants. *Proc. Natl. Acad. Sci.* **2018**, *115*, E822–E831.
28. Corson, F.; Hamant, O.; Bohn, S.; Traas, J.; Boudaoud, A.; Couder, Y. Turning a plant tissue into a living cell froth through isotropic growth. *Proc. Natl. Acad. Sci. U. S. A.* **2009**, *106*, 8453–8458.
29. Ishihara, S.; Sugimura, K.; Cox, S.J.; Bonnet, I.; Bellaïche, Y.; Graner, F. Comparative study of non-invasive force and stress inference methods in tissue. *Eur. Phys. J. E Soft Matter* **2013**, *36*, 9859.
30. Cheddadi, I.; Génard, M.; Bertin, N.; Godin, C. Coupling water fluxes with cell wall mechanics in a multicellular model of plant development. *PLOS Comput. Biol.* **2019**, *15*, e1007121.
31. Lucas, W.J.; Ham, B.-K.; Kim, J.-Y. Plasmodesmata - bridging the gap between neighboring plant cells. *Trends Cell Biol.* **2009**, *19*, 495–503.
32. Kumar, N.M.; Gilula, N.B. The Gap Junction Communication Channel. *Cell* **1996**, *84*, 381–388.
33. McLean, P.F.; Cooley, L. Protein Equilibration through Somatic Ring Canals in Drosophila. *Science* **2013**, *340*.
34. Willis, L.; Refahi, Y.; Wightman, R.; Landrein, B.; Teles, J.; Huang, K.C.; Meyerowitz, E.M.; Jönsson, H. Cell size and growth regulation in the Arabidopsis thaliana apical stem cell niche. *Proc. Natl. Acad. Sci. U. S. A.* **2016**, *113*, E8238–E8246.
35. Boyer, J.S.; Cavalieri, A.J.; Schulze, E.-D. Control of the rate of cell enlargement: Excision, wall relaxation, and growth-induced water potentials. *Planta* **1985**, *163*, 527–543.
36. Cosgrove, D.J. Cell Wall Yield Properties of Growing Tissue: Evaluation by in Vivo Stress Relaxation. *Plant Physiol.* **1985**, *78*, 347–356.
37. Ortega, J.K.E. Dimensionless Numbers to Analyze Expansive Growth Processes. *Plants* **2019**, *8*, 17.
38. Vella, D.; Ajdari, A.; Vaziri, A.; Boudaoud, A. The indentation of pressurized elastic shells: from polymeric capsules to yeast cells. *J. R. Soc. Interface* **2012**, *9*, 448–455.
39. Vella, D.; Ajdari, A.; Vaziri, A.; Boudaoud, A. Indentation of Ellipsoidal and Cylindrical Elastic Shells. *Phys. Rev. Lett.* **2012**, *109*, 144302.

40. Beauzamy, L.; Derr, J.; Boudaoud, A. Quantifying Hydrostatic Pressure in Plant Cells by Using Indentation with an Atomic Force Microscope. *Biophys. J.* **2015**, *108*, 2448–2456.
41. Beauzamy, L.; Louveaux, M.; Hamant, O.; Boudaoud, A. Mechanically, the Shoot Apical Meristem of Arabidopsis Behaves like a Shell Inflated by a Pressure of About 1 MPa. *Front. Plant Sci.* **2015**, *6*.
42. Malgat, R.; Faure, F.; Boudaoud, A. A Mechanical Model to Interpret Cell-Scale Indentation Experiments on Plant Tissues in Terms of Cell Wall Elasticity and Turgor Pressure. *Front. Plant Sci.* **2016**, *7*.
43. Lazarus, A.; Florijn, H.C.B.; Reis, P.M. Geometry-induced rigidity in nonspherical pressurized elastic shells. *Phys. Rev. Lett.* **2012**, *109*, 144301.
44. Kierzkowski, D.; Nakayama, N.; Routier-Kierzkowska, A.-L.; Weber, A.; Bayer, E.; Schorderet, M.; Reinhardt, D.; Kuhlemeier, C.; Smith, R.S. Elastic domains regulate growth and organogenesis in the plant shoot apical meristem. *Science* **2012**, *335*, 1096–1099.
45. Milani, P.; Gholamirad, M.; Traas, J.; Arnéodo, A.; Boudaoud, A.; Argoul, F.; Hamant, O. In vivo analysis of local wall stiffness at the shoot apical meristem in Arabidopsis using atomic force microscopy. *Plant J. Cell Mol. Biol.* **2011**, *67*, 1116–1123.
46. Mosca, G.; Sapala, A.; Strauss, S.; Routier-Kierzkowska, A.-L.; Smith, R.S. On the micro-indentation of plant cells in a tissue context. *Phys. Biol.* **2017**, *14*, 015003.
47. Hong, L.; Dumond, M.; Tsugawa, S.; Sapala, A.; Routier-Kierzkowska, A.-L.; Zhou, Y.; Chen, C.; Kiss, A.; Zhu, M.; Hamant, O.; et al. Variable Cell Growth Yields Reproducible Organ Development through Spatiotemporal Averaging. *Dev. Cell* **2016**, *38*, 15–32.
48. Yi, H.; Chen, Y.; Wang, J.Z.; Puri, V.M.; Anderson, C.T. The stomatal flexoskeleton: how the biomechanics of guard cell walls animate an elastic pressure vessel. *J. Exp. Bot.* **2019**, *70*, 3561–3572.
49. Knoblauch, J.; Mullendore, D.L.; Jensen, K.H.; Knoblauch, M. Pico gauges for minimally invasive intracellular hydrostatic pressure measurements. *Plant Physiol.* **2014**, pp.114.245746.
50. Nakayama, N.; Smith, R.S.; Mandel, T.; Robinson, S.; Kimura, S.; Boudaoud, A.; Kuhlemeier, C. Mechanical Regulation of Auxin-Mediated Growth. *Curr. Biol.* **2012**, *22*, 1468–1476.
51. Lewis, F.T. The correlation between cell division and the shapes and sizes of prismatic cells in the epidermis of cucumis. *Anat. Rec.* **1928**, *38*, 341–376.
52. Gibson, W.T.; Veldhuis, J.H.; Rubinstein, B.; Cartwright, H.N.; Perrimon, N.; Brodland, G.W.; Nagpal, R.; Gibson, M.C. Control of the mitotic cleavage plane by local epithelial topology. *Cell* **2011**, *144*, 427–438.
53. Hamant, O.; Heisler, M.G.; Jönsson, H.; Krupinski, P.; Uyttewaal, M.; Bokov, P.; Corson, F.; Sahlin, P.; Boudaoud, A.; Meyerowitz, E.M.; et al. Developmental Patterning by Mechanical Signals in Arabidopsis. *Science* **2008**, *322*, 1650–1655.
54. Kwiatkowska, D. Surface growth at the reproductive shoot apex of Arabidopsis thaliana pin-formed 1 and wild type. *J. Exp. Bot.* **2004**, *55*, 1021–1032.
55. Serrano-Mislata, A.; Schiessl, K.; Sablowski, R. Active Control of Cell Size Generates Spatial Detail during Plant Organogenesis. *Curr. Biol.* **2015**, *25*, 2991–2996.
56. Ali, O.; Mirabet, V.; Godin, C.; Traas, J. Physical models of plant development. *Annu. Rev. Cell Dev. Biol.* **2014**, *30*, 59–78.
57. Dumond, M.; Boudaoud, A. Physical Models of Plant Morphogenesis. In *Mathematical*

Modelling in Plant Biology; Morris, R.J., Ed.; Springer International Publishing: Cham, 2018; pp. 1–14 ISBN 978-3-319-99070-5.

58. Alt, S.; Ganguly, P.; Salbreux, G. Vertex models: from cell mechanics to tissue morphogenesis. *Philos. Trans. R. Soc. B Biol. Sci.* **2017**, *372*.
59. Dyson, R.J.; Vizcay-Barrena, G.; Band, L.R.; Fernandes, A.N.; French, A.P.; Fozard, J.A.; Hodgman, T.C.; Kenobi, K.; Pridmore, T.P.; Stout, M.; et al. Mechanical modelling quantifies the functional importance of outer tissue layers during root elongation and bending. *New Phytol.* **2014**, *202*, 1212–1222.
60. Forouzesh, E.; Goel, A.; Mackenzie, S.A.; Turner, J.A. In vivo extraction of Arabidopsis cell turgor pressure using nanoindentation in conjunction with finite element modeling. *Plant J.* **2013**, *73*, 509–520.
61. Maurel, C.; Boursiac, Y.; Luu, D.-T.; Santoni, V.; Shahzad, Z.; Verdoucq, L. Aquaporins in Plants. *Physiol. Rev.* **2015**, *95*, 1321–1358.
62. Klepikova, A.V.; Kasianov, A.S.; Gerasimov, E.S.; Logacheva, M.D.; Penin, A.A. A high resolution map of the Arabidopsis thaliana developmental transcriptome based on RNA-seq profiling. *Plant J. Cell Mol. Biol.* **2016**, *88*, 1058–1070.
63. Péret, B.; Li, G.; Zhao, J.; Band, L.R.; Voß, U.; Postaire, O.; Luu, D.-T.; Da Ines, O.; Casimiro, I.; Lucas, M.; et al. Auxin regulates aquaporin function to facilitate lateral root emergence. *Nat. Cell Biol.* **2012**, *14*, 991–998.
64. Tsugawa, S.; Hervieux, N.; Kierzkowski, D.; Routier-Kierzkowska, A.-L.; Sapala, A.; Hamant, O.; Smith, R.S.; Roeder, A.H.K.; Boudaoud, A.; Li, C.-B. Clones of cells switch from reduction to enhancement of size variability in Arabidopsis sepals. *Development* **2017**, *144*, 4398–4405.
65. Sapala, A.; Runions, A.; Routier-Kierzkowska, A.-L.; Das Gupta, M.; Hong, L.; Hofhuis, H.; Verger, S.; Mosca, G.; Li, C.-B.; Hay, A.; et al. Why plants make puzzle cells, and how their shape emerges. *eLife* **2018**, *7*.
66. LeGoff, L.; Rouault, H.; Lecuit, T. A global pattern of mechanical stress polarizes cell divisions and cell shape in the growing Drosophila wing disc. *Development* **2013**, *140*, 4051–4059.
67. Campinho, P.; Behrndt, M.; Ranft, J.; Risler, T.; Minc, N.; Heisenberg, C.-P. Tension-oriented cell divisions limit anisotropic tissue tension in epithelial spreading during zebrafish epiboly. *Nat. Cell Biol.* **2013**, *15*, 1405–1414.
68. Mao, Y.; Tournier, A.L.; Hoppe, A.; Kester, L.; Thompson, B.J.; Tapon, N. Differential proliferation rates generate patterns of mechanical tension that orient tissue growth. *EMBO J.* **2013**, *32*, 2790–2803.
69. Louveaux, M.; Julien, J.-D.; Mirabet, V.; Boudaoud, A.; Hamant, O. Cell division plane orientation based on tensile stress in Arabidopsis thaliana. *Proc. Natl. Acad. Sci.* **2016**, *113*, E4294–E4303.
70. Gibson, W.T.; Gibson, M.C. Chapter 4 Cell Topology, Geometry, and Morphogenesis in Proliferating Epithelia. In *Current Topics in Developmental Biology*; Current Topics in Developmental Biology; Academic Press, 2009; Vol. 89, pp. 87–114.
71. Long, Y.; Boudaoud, A. Emergence of robust patterns from local rules during plant development. *Curr. Opin. Plant Biol.* **2018**, *47*, 127–137.
72. Vargas-Garcia, C.A.; Ghusinga, K.R.; Singh, A. Cell size control and gene expression homeostasis in single-cells. *Curr. Opin. Syst. Biol.* **2018**, *8*, 109–116.
73. Cutler, S.R.; Ehrhardt, D.W.; Griffitts, J.S.; Somerville, C.R. Random GFP::cDNA fusions enable

933 visualization of subcellular structures in cells of Arabidopsis at a high frequency. *Proc. Natl.*
934 *Acad. Sci.* **2000**, *97*, 3718–3723.
935 74. Stanislas, T.; Hamant, O.; Traas, J. Chapter 11 - In-vivo analysis of morphogenesis in plants. In
936 *Methods in Cell Biology*; Lecuit, T., Ed.; Cell Polarity and Morphogenesis; Academic Press,
937 2017; Vol. 139, pp. 203–223.
938 75. Reuille, P.B. de; Bohn-Courseau, I.; Godin, C.; Traas, J. A protocol to analyse cellular dynamics
939 during plant development. *Plant J.* **2005**, *44*, 1045–1053.
940 76. Legland, D.; Arganda-Carreras, I.; Andrey, P. MorphoLibJ: integrated library and plugins for
941 mathematical morphology with ImageJ. *Bioinformatics* **2016**, *32*, 3532–3534.
942 77. Mirabet, V.; Dubrulle, N.; Rambaud, L.; Beauzamy, L.; Dumond, M.; Long, Y.; Milani, P.;
943 Boudaoud, A. NanoIndentation, an ImageJ Plugin for the Quantification of Cell Mechanics.
944 *Methods Mol. Biol.* **in press**.
945 78. Sassi, M.; Ali, O.; Boudon, F.; Cloarec, G.; Abad, U.; Cellier, C.; Chen, X.; Gilles, B.; Milani, P.;
946 Friml, J.; et al. An auxin-mediated shift toward growth isotropy promotes organ formation at
947 the shoot meristem in Arabidopsis. *Curr. Biol. CB* **2014**, *24*, 2335–2342.
948 79. Kremer, A.; Lippens, S.; Bartunkova, S.; Asselbergh, B.; Blanpain, C.; Fendrych, M.; Goossens,
949 A.; Holt, M.; Janssens, S.; Krols, M.; et al. Developing 3D SEM in a broad biological context. *J.*
950 *Microsc.* **2015**, *259*, 80–96.
951 80. Kiss, A.; Moreau, T.; Mirabet, V.; Calugaru, C.I.; Boudaoud, A.; Das, P. Segmentation of 3D
952 images of plant tissues at multiple scales using the level set method. *Plant Methods* **2017**,
953 *13*, 114.
954 81. Reuille, P.B. de; Routier-Kierzkowska, A.-L.; Kierzkowski, D.; Bassel, G.W.; Schüpbach, T.;
955 Tauriello, G.; Bajpai, N.; Strauss, S.; Weber, A.; Kiss, A.; et al. MorphoGraphX: A platform for
956 quantifying morphogenesis in 4D. *eLife* **2015**, *4*, e05864.
957 82. Schmidt, T.; Pasternak, T.; Liu, K.; Blein, T.; Aubry-Hivet, D.; Dovzhenko, A.; Duerr, J.; Teale, W.;
958 Ditengou, F.A.; Burkhardt, H.; et al. The iRoCS Toolbox – 3D analysis of the plant root apical
959 meristem at cellular resolution. *Plant J.* **2014**, *77*, 806–814.

960